2009-12

Investigation of shock wave attenuation in porous materials

Boey, Chung Wai.

Monterey, California. Naval Postgraduate School

NAVAL POSTGRADUATE SCHOOL

MONTEREY, CALIFORNIA

THESIS

INVESTIGATION OF SHOCK WAVE ATTENUATION IN POROUS MATERIALS

by

Boey Chung Wai

December 2009

Thesis Advisor:	Robert S. Hixson
Second Reader:	Terry McNelley

Approved for public release; distribution is unlimited

THIS PAGE INTENTIONALLY LEFT BLANK

REPORT DOCUMENTATION PAGE			Form Approved OMB No. 0704-0188
Public reporting burden for this collection of information is estimated to average 1 hour per response, including the time for reviewing instruction, searching existing data sources, gathering and maintaining the data needed, and completing and reviewing the collection of information. Send comments regarding this burden estimate or any other aspect of this collection of information, including suggestions for reducing this burden, to Washington headquarters Services, Directorate for Information Operations and Reports, 1215 Jefferson Davis Highway, Suite 1204, Arlington, VA 22202-4302, and to the Office of Management and Budget, Paperwork Reduction Project (0704-0188) Washington DC 20503.			
1. AGENCY USE ONLY *(Leave blank)*	**2. REPORT DATE** December 2009	**3. REPORT TYPE AND DATES COVERED** Master's Thesis	
4. TITLE AND SUBTITLE Investigation of Shock Wave Attenuation in Porous Materials		**5. FUNDING NUMBERS**	
6. AUTHOR(S) Boey Chung Wai			
7. PERFORMING ORGANIZATION NAME(S) AND ADDRESS(ES) Naval Postgraduate School Monterey, CA 93943-5000		**8. PERFORMING ORGANIZATION REPORT NUMBER**	
9. SPONSORING /MONITORING AGENCY NAME(S) AND ADDRESS(ES) N/A		**10. SPONSORING/MONITORING AGENCY REPORT NUMBER**	
11. SUPPLEMENTARY NOTES The views expressed in this thesis are those of the author and do not reflect the official policy or position of the Department of Defense or the U.S. Government.			
12a. DISTRIBUTION / AVAILABILITY STATEMENT Approved for public release; distribution is unlimited		**12b. DISTRIBUTION CODE**	

13. ABSTRACT (maximum 200 words)

This thesis investigates the use of porous materials in a multi-layered armor concept. The prototype layered structure consists of an initial high-strength material to slow down the projectile and cause significant plastic deformation,, followed by an orthotropic wave-spreading layer to spread shock waves laterally away from the axis of penetration and subsequently attenuate the shock waves by using a porous material to convert kinetic energy into internal energy. Based on the above armor concept, composite plates consisted of an alumina (Al_20_3)-based ceramic, Dyneema® and porous foams were constructed and tested against conventional armor steel of equivalent areal density. This study used two commercially available porous materials, one based on aluminum metal and one a rigid polyurethane foam. This study also investigated the effect of porous initial density of the polymeric foam on ballistic. The author developed a P-α compaction model for the chosen porous materials for use in AUTODYN® simulations to describe their dynamic compaction during an impact event. The author also conducted a ballistic trial to validate the performance of the armor laminate against numerical simulations. Based on the results of this study, the porous layer has proven to be a good shock attenuator. The porous material efficiently delays the shock wave propagation and attenuates the amplitude by absorbing the kinetic energy through compaction of the material. The current research has also proven that the material layering sequence is fundamentally correct and has its merits.

14. SUBJECT TERMS Porous Foams, Dynamic Compaction, Multi-layered Armor, Ballistic Performance, Shock Wave Attenuation			**15. NUMBER OF PAGES** 107
			16. PRICE CODE
17. SECURITY CLASSIFICATION OF REPORT Unclassified	**18. SECURITY CLASSIFICATION OF THIS PAGE** Unclassified	**19. SECURITY CLASSIFICATION OF ABSTRACT** Unclassified	**20. LIMITATION OF ABSTRACT** UU

NSN 7540-01-280-5500 Standard Form 298 (Rev. 8-98)
Prescribed by ANSI Std. Z39.18

THIS PAGE INTENTIONALLY LEFT BLANK

Approved for public release; distribution is unlimited

INVESTIGATION OF SHOCK WAVE ATTENUATION IN POROUS MATERIALS

Boey Chung Wai
Civilian, Singapore Technologies Dynamics, Ltd
B. S., National University of Singapore, 1999

Submitted in partial fulfillment of the
requirements for the degree of

MASTER OF SCIENCE IN MECHANICAL ENGINEERING

from the

NAVAL POSTGRADUATE SCHOOL
December 2009

Author: Boey Chung Wai

Approved by: Professor Robert S. Hixson
Thesis Advisor

Professor Terry McNelley
Second Reader

Professor Knox Millsaps
Chairman, Department of Mechanical and Astronautical Engineering

THIS PAGE INTENTIONALLY LEFT BLANK

ABSTRACT

This thesis investigates the use of porous materials in a multi-layered armor concept. The prototype layered structure consists of an initial high-strength material to slow down the projectile and cause significant plastic deformation, followed by an orthotropic wave-spreading layer to spread shock waves laterally away from the axis of penetration and subsequently attenuate the shock waves by using a porous material to convert kinetic energy into internal energy. Based on the above armor concept, composite plates consisted of an alumina (Al_20_3)-based ceramic, Dyneema® and porous foams were constructed and tested against conventional armor steel of equivalent areal density. This study used two commercially available porous materials, one based on aluminum metal and one a rigid polyurethane foam. This study also investigated the effect of porous initial density of the polymeric foam on ballistic. The author developed a P-α compaction model for the chosen porous materials for use in AUTODYN® simulations to describe their dynamic compaction during an impact event. The author also conducted a ballistic trial to validate the performance of the armor laminate against numerical simulations. Based on the results of this study, the porous layer has proven to be a good shock attenuator. The porous material efficiently delays the shock wave propagation and attenuates the amplitude by absorbing the kinetic energy through compaction of the material. The current research has also proven that the material layering sequence is fundamentally correct and has its merits.

THIS PAGE INTENTIONALLY LEFT BLANK

TABLE OF CONTENTS

LIST OF FIGURES

LIST OF TABLES

THIS PAGE INTENTIONALLY LEFT BLANK

ACKNOWLEDGMENTS

Though the following dissertation is an individual work, completion of my research would not be possible without the guidance of my professors, help from friends, and support from my family and wife.

I would like to express my deepest gratitude to Professor Hixson for offering his invaluable guidance, time, patience, wealth of experience, and knowledge that has made this a wonderful learning experience for me. I would also like to thank Professor McNelley, Professor Jose O Sinibaldi, Dr. Menon, and Dr. Chanman Park who are always available and patient in providing suggestions and advice for my research. Special thanks go to Kirk Fields, Nell Gamble, and Brett Compton of the Mechanical Engineering Department of UCSB for their time and help in conducting the gas-gun experiments. I would also like to thank my research partner, Roy, who as a good friend was always willing to help and give his best suggestions. Last, but not least, I would like to thank my wife, Sharon, for her unwavering support throughout my time in NPS.

THIS PAGE INTENTIONALLY LEFT BLANK

I. INTRODUCTION

A. MOTIVATION

With ever-increasing ballistic threats and survivability requirements, coupled with the need for high tactical mobility of future combat systems, research on lightweight armor systems continues to be of interest to many military forces around the world. In order to optimize the weight/performance ratio of armor systems for both personnel and vehicles, it is important to understand at a very fundamental level how they respond to ballistic impacts. Achieving a reduction in armor weight coupled with improved ballistic performance will require the use of new materials or combinations of materials, a better fundamental understanding of stress wave propagation across dissimilar materials, the optimization of competing performance requirements, and an improved understanding of damage mechanisms of new ballistic threats. Taken together, this means that there is still a need for innovative armor concepts.

There has been a considerable evolution in armor technology for personnel and vehicles since World War II. However, most passive armor systems have focused on the use of very strong materials to disrupt the incoming threat by breaking up or deforming the projectile. Hardened steel or rolled homogeneous armor (RHA) continue to be popular choices, especially for armored vehicles because of overall good ballistic performance and its relatively low cost. The use of RHA as a benchmark for new armor systems still occurs today. However, at high impact velocities, due to the short timeframe and highly localized nature of the impact, the material strength of such strong materials is vey small when compared to the compressive and tensile stresses generated upon impact. Hence, there can be considerable damage inflicted on the target. To effectively defeat a projectile without experiencing high material stress, armor materials designed to attenuate impact generated shock waves, and absorbs the kinetic energy of the projectile and converts it to another form of energy, i.e.,

heat, can effectively mitigate the penetration process. Porous materials possess good shock absorption properties, which make them light energy absorbers, potentially suitable for lightweight armor applications.

B. RESEARCH GOAL

The goal of this research is to investigate the use of porous materials in a layered structure for advanced armor protection. The current work is a continuation of thesis work completed by Poh [1]. As there is currently no single material that can be optimized to both disrupt and absorb the kinetic energy of an incoming threat, Poh [1] had introduced the concept of an integrated multi-layered structure to enable sharing of functions among the various material constituents to optimize ballistic performance for improved survivability. The layered structure (see Figure 1) consists of an initial high-strength material to slow down the projectile and cause significant plastic deformation, followed by an orthotropic wave-spreading layer to spread the shock waves laterally away from the axis of penetration and subsequently attenuate them by absorbing the kinetic energy through compaction of the porous layer. Poh [1] had clearly shown through numerical simulation using theoretically desirable material properties that the layered structure concept has its merits.

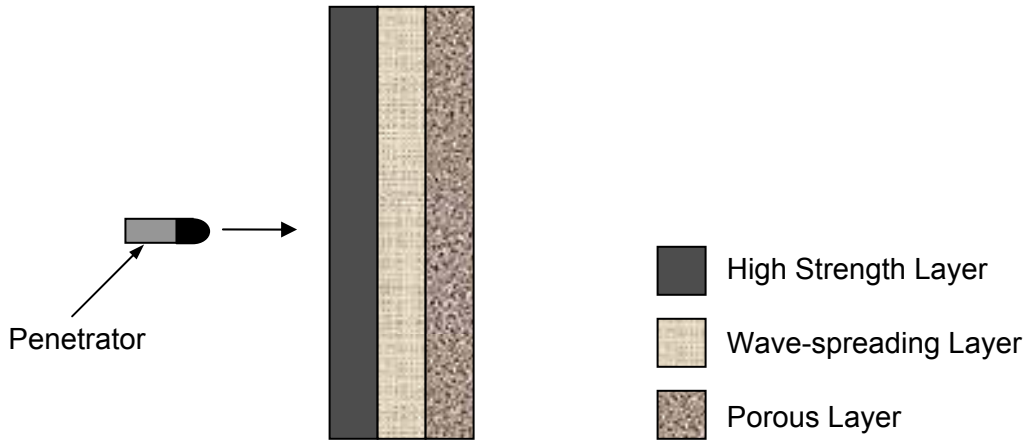

Figure 1. Multi-layered Structure Armor Concept

The goal of this research is to better understand the basic shock physics response of a similar concept and develop a hydrocode model, which can predict the ballistic performance to identify material properties in order to optimize the armor design for performance/weight ratio. In particular, this study can address the effect of pore size and void volume of the porous material on overall ballistic performance. In future research, with better understanding of shock wave propagation across dissimilar materials, there could be the development of a single material with multi-functional roles to integrate the roles currently fulfilled by each individual material layer.

C. RESEARCH OBJECTIVES

Since the work done by Poh [1] has shown through numerical modeling that the multi-layered structure armor concept has its merits, the current research objective is to refine the design and prove the concept experimentally through ballistic trials using commercially available materials to form the layered structure. The focus of this thesis is on the porous layer. Concurrent thesis work by Ong [2] focuses on the wave-spreading layer.

The author selected two commercially available porous materials, namely aluminum metal foam and rigid polyurethane foam, and performed material characterization. He also investigated Polyurethane foam of two different densities. The author performed numerical modeling using the AUTODYN® hydrocode in conjunction with ballistic trials to better understand the two-dimensional response and shock physics of the porous material in the laminate configuration described above. He then compared and validated the simulation predictions against the field trial results in terms of deformation, damage, and ballistic performance. As there is currently a wide range of ballistic threats, the author recognizes the limits to the effectiveness of his armor design against each individual threat. Hence, the current study focuses on small arms threats for

personnel and lightweight vehicle armor. Then, there can be a suitable scaling of the proven concept to meet the ever-changing battlefield survivability requirements.

II. BACKGROUND

A. INTRODUCTION

The use of porous materials in shock absorption and isolation applications is extensive because of their effectiveness in attenuating shock and mitigating impact pressure. A porous medium or material is a solid permeated by an interconnected network of pores (voids) filled with a fluid (liquid or gas) [3]. The pores distend the solid material, causing it to have an initial density lower than the crystalline density. Due to their effectiveness in energy absorption for protection applications, such materials continue to be of interest. However, most current applications have been restricted to relatively low velocity impacts.

Recent experimental studies [4] have demonstrated that a porous material such as polyurethane foam can cause peak overpressure attenuation of a blast wave by 10-50% as compared to air as a medium. Current potential military applications include using rigid polyurethane foam (RPF) for mine protection. The results of explosive experiments show that RPF is effective in absorbing direct blast waves from explosives. Beyond that application, the foam is also effective in reducing the signature of vehicles passing over anti-tank (AT) mines to prevent the mine from firing. Further investigations for field applications are currently on-going [5]. Recent experimental work on low-density aluminum foam, as a backing plate for ceramic in composite armor, has revealed improved ballistic performance with the foam exhibiting significant non-linear deformation and stress wave attenuation. The superior performance and unique attributes of porous materials may allow a significant advancement towards lighter and more damage-tolerant composite integral armor for the next generation of lightweight armored vehicles [6].

B. DYNAMIC COMPACTION OF POROUS MATERIALS

In order to exploit the unique properties of porous materials, it is important to understand their behavior when subjected to dynamic compaction. Porous materials respond quite differently from their solid parent material when subjected to a shock or dynamic compression. For solid materials (see Figure 2) subjected to small strains and stresses, the shock Hugoniot and the ambient isentrope are similar. Hence, for qualitative purposes, one can assume that the Hugoniot is the release path for a material subjected to shock compression with only a small error. When a solid material is subjected to a shock from its initial rest condition P_0,V_0 during the shock compression process from initial state to the final state P,V, the material shock response follows the Rayleigh line. However, when the pressure is released, the material follows the shock Hugoniot curve, which is an approximation following the released isentrope, down in stress. The resulting observation is that the shock process is irreversible as the internal energy increase due to the shock process, which is proportional to the area under the Rayleigh line, is not completely recovered upon release and hence, the material is left with some residual energy, usually in the form of heat [7].

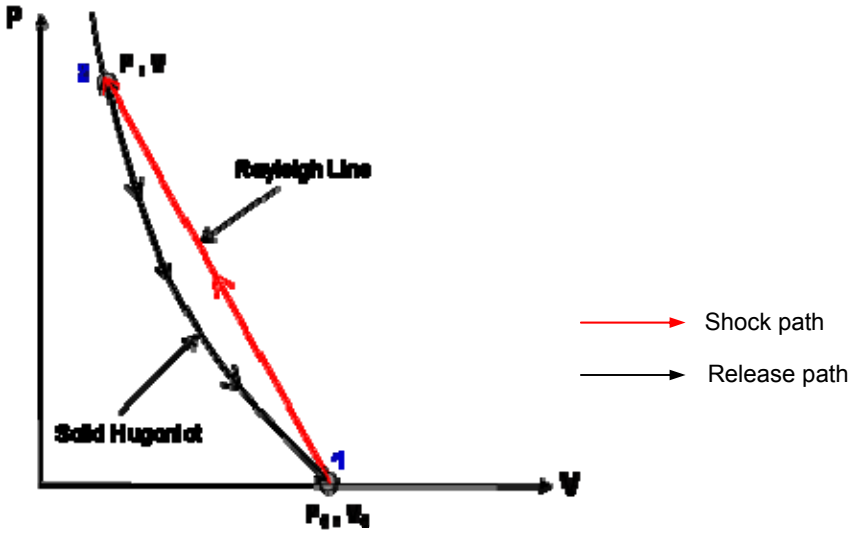

Figure 2. Shock Compression Behavior of Solid Materials

For porous materials (see Figure 3), since the material is distended, its initial volume is larger than the full density initial volume. The inclusion of porosity in the matrix of the solid material allows for the attainment of larger initial volumes. When subjected to shock compression, the material (assumed here to have no strength) will follow the Rayleigh line from the distended initial volume to the final state (diagonal path), and if the shock stress is high enough, approach the full density solid Hugoniot. During the compression from 1 to 2, the pores in the distended material are completely crushed out, and this path is known as the crush curve. The pores will remain crushed once crushed. Hence, when the pressure is released, the material will approximately follow the Hugoniot down to final state 4, which has a smaller ambient volume than the initial distended volume at 1 [7]. The shock compression process therefore crushes out the pores and leads to permanent material densification. The release path from state 2 is really an isentrope centered on the entropy increase that happens in the shock compression process. This isentrope will be close to the Hugoniot only when a small entropy increase occurs in the shock compression process. The author makes this assumption here to be able to *qualitatively* understand the shock/release process.

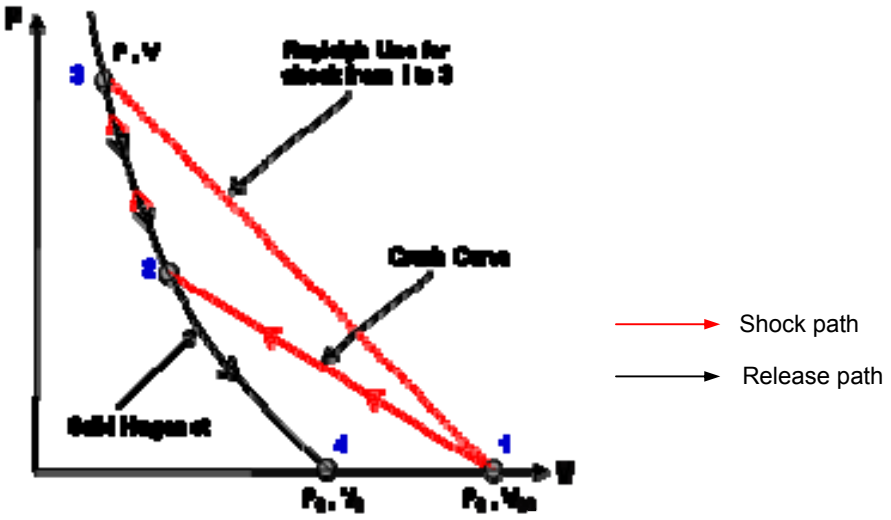

Figure 3. Shock Compression Behavior of Porous Materials

Due to their distended volume, as compared to fully dense solid materials, there is a much greater internal energy increase behind a shock in a porous material compared to a solid material (see Figure 4). Porous materials can absorb kinetic energy when the pores collapse so their internal energy, density, and temperature all increase through p-v work. In the process of pore collapse, the material can strongly attenuate shock waves, and the kinetic energy is absorbed and turned into waste heat [7]. As mentioned earlier, the shock process is irreversible and some fraction of the internal energy increase realized in the compression is not recovered upon release of pressure. Some of this energy is left behind as waste heat, causing the final temperature to be greater than the initial temperature. It is a well-known fact that porous materials increase in temperature very quickly when shocked, much more quickly than solid matrix material alone. This can cause melting and even vaporization at much lower stress than for solid materials. Hence, it is clear that there is much more energy absorbed or residual energy left behind for the porous material compared to the full density solid material. The presence of pores makes porous materials good mechanical energy absorbers.

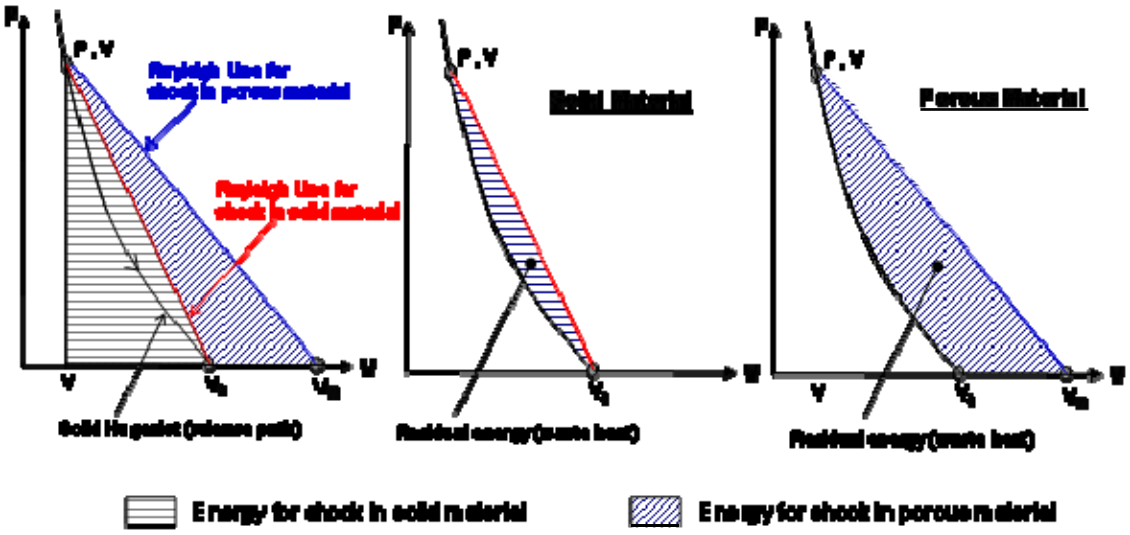

Figure 4. Energy Absorption Characteristics of Porous Material

A stress-strain diagram illustrates the energy absorption characteristics of porous materials [3]. The stress-strain plot can be divided into three regions (see Figure 5):

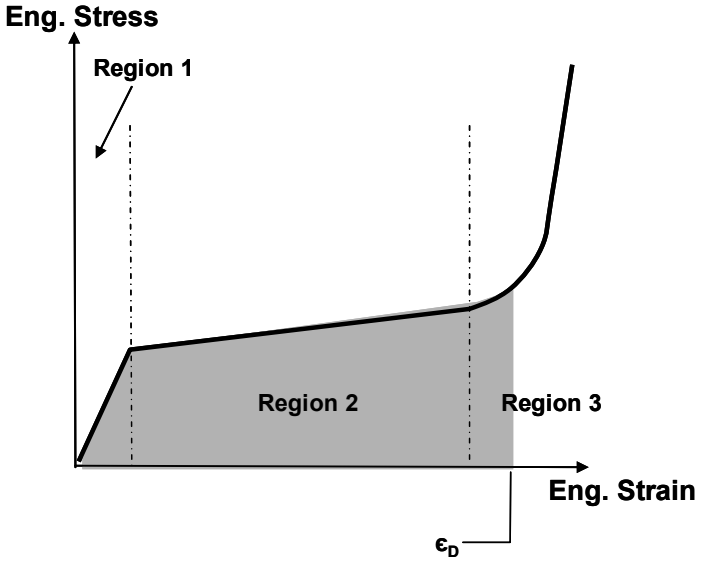

Figure 5. Stress-strain Behavior of Porous Material

Region 1

Region 1 is known as the linear elastic region. Under low pressure (or stress) conditions, only elastic deformation occurs. The temporary shape change is recoverable after the load is removed and the material returns to its original shape. This type of deformation involves only stretching or elastic compression of the atom-atom bonds. The slope of the plot at this region is defined as the Young's modulus, which is a measure of the stiffness of an isotropic elastic material.

Region 2

When there is sufficient stress to permanently deform the material, plastic deformation occurs. This is when the first cell wall (or pore) collapse occurs. Hence, this is known as the collapse region. When the material is compressed beyond this yield point, upon release of the applied load the material returns to

zero stress (relaxed state) along an elastic path, resulting in a residual strain or permanent shape change. This means that there is hysteresis in the stress strain response.

Region 3

As the porous material progressively collapses, densification occurs, i.e., volume is reduced. This is known as the densification region. Densification occurs up to the densification strain ϵ_D. At strain values beyond ϵ_D, the structure is completely compacted, the stress rises steeply, and the material behaves like a fully dense material. The area under the stress-strain curve (up to the densification strain) is proportional to the energy the porous material can absorb and is the energy-absorbing performance indicator of the porous material. Hence, it is desirable for the material to posses a large ϵ_D for energy absorption applications.

Some behavioral properties of porous materials during dynamic compaction can also be determined analytically using conservation equations. The shock and particle velocity for a porous material can be determined by using the jump conditions to derive a relationship between pressure and run distance or time. The derived relationship reveals that the pressure drops with distance as $1/x^2$, and with time as 1/t. This shows the dispersive nature of porous materials, which makes them good shock wave attenuators [7].

C. COMPACTION MODELS

To better understand the behavior of a shock-compressed porous material through numerical modeling, constitutive models have been developed to model the compression of porous materials. The earliest and simplest model is the snowplow model (relating porous material compaction to snow compaction). In this model, the assumption is that there is no resistance to compaction. The solid Hugoniot is vertical which means that the end state for compression is always the same volume. Hence, the snowplow model is appropriate only to

describe porous materials that completely crush when subjected to any shock (see Figure 6) [7]. However, in reality, most porous materials offer some resistance to compaction, and thus exhibit some form of partial compaction.

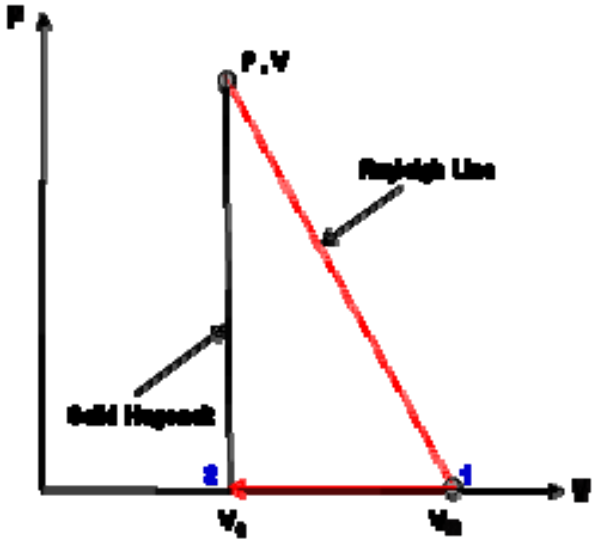

Figure 6. Snowplow Compaction Model

As the snowplow model does not allow for partial compaction, another porous compaction model known as the P-α model is more commonly used, as to be able to describe partially compacted states. W. Herrmann initially developed the irreversible P-α compaction model in 1969 [8] to provide a mechanism to describe the behavior of slightly distended material. Since then, there has been a successful extension of the model to materials with much larger distensions [9]. A porosity parameter, α, has been introduced to allow for the convenient separation of volume change due to compression of the material from that due to pore collapse.

$$\text{Porosity, } \alpha = \frac{V}{V_s}$$

where V is the specific volume of porous material and V_s is the specific volume of the corresponding solid material at the same temperature and pressure. Note that porosity, α, becomes unity when the material is solid.

The P-α compaction model describes the dynamic compaction of a porous material [9], as shown in Figure 7. There are several stages to the compression and release of materials in this model:

a. Initial elastic compression is governed by elastic buckling of cell walls.

b. The beginning of permanent volume change coincides with the start of plastic deformation of the cell wall at pressure P_e (which is the yield strength of the porous material)

c. Dynamic compaction then moves along Rayleigh lines to end states on the plastic curve (described by the equation) until the pressure reaches the fully compacted state at the solid compaction pressure P_s or is released to a partially compacted state.

d. Unloading from a partially compacted state is elastic with its end state at a smaller ambient specific volume than the starting volume due to localized densification.

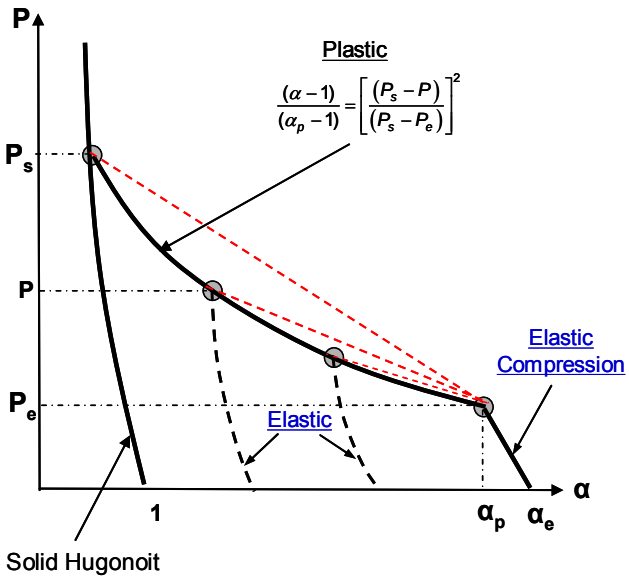

Figure 7. P-α Compaction Model

This model is the simplest model that can realistically describe the shock compression and release process in porous materials. This model also adequately describes the release from partially compacted states, which is important for low-stress applications. Because of this, the P-α model is widely

used in the dynamic materials community, and is widely used in hydrodynamic computer code simulations. More advanced models exist, but they are typically more complicated and computationally intensive. For this reason, the author has chosen to use the P-α model.

THIS PAGE INTENTIONALLY LEFT BLANK

III. HYDROCODE SIMULATIONS

A. AUTODYN® HYDROCODE

A hydrocode is a numerical computer program that uses a combination of finite difference and finite element techniques to solve dynamic problems that occur in a short time scale [10], [11]. Examples of such problems include kinetic energy penetration phenomena, for example, a projectile or bullet impacting a barrier. For this study, the author uses the AUTODYN®2D hydrocode (by Century Dynamics) to model the non-linear behavior of a projectile impacting a multi-layered structure so he can model its ballistic performance. He performs the numerical computation in AUTODYN® using the governing equations of conservation of mass, momentum and energy, as defined in the Euler equations. In addition, there must be specification of the material's equation of state and a suitable constitutive strength model to accurately describe the response of solid materials and their behavior when subjected to transient shock loads. As for all numerically different computer codes, artificial viscosity is used to damp out numerical instabilities that can arise for the particular differencing technique used. Although there is a need for artificial viscosity to achieve stable calculations, this can lead to slight errors in stress and energy.

B. GENERAL HYDROCODE SETTINGS

There are several critical settings available in AUTODYN® for setting up a simulation. Some of the discussed settings will determine how accurately the simulations model the actual scenario.

1. Meshing Description

In hydrocodes, there are two main types of grid systems used to describe material movement, namely the Lagrange and Euler system. The author uses the Lagrange system in the numerical simulations in this study. Unlike an

Eulerian code which has a fixed grid, the Lagrange code has a grid embedded with the material, and as the code tracks the flow or motion of individual masses, the grid deforms together with the material. Hence, Lagrange codes are simpler and require fewer computations since they do not require a transport algorithm to move material to neighboring cells. However, Lagrange codes have problems with accurately tracking large deformations. With large deformations, numerical problems arising from grid distortion and tangling of the mesh can lead to loss of accuracy and time steps becoming small enough to terminate computation. To overcome this, and especially for highly localized distortions, an erosion algorithm has to be implemented. The erosion algorithm removes the distorted grid elements when they reach a predefined criterion, which is normally some value of plastic strain. This allows the computation to continue, but there is no preservation of the conservation of energy since there is no longer tracking of the internal energy of the failed elements. However, previous studies have shown that close agreement between calculations employing erosion techniques and experimental results can be achieved [12].

2. Simulation Setup

The author uses a 2D axisymmetric geometry in the calculations so that he can complete the simulation in a reasonable time. In numerical analyses of dynamic loading, it is necessary to use fine meshes to ensure the accuracy of the results. However, simulations using short element lengths are computationally intensive and take much longer time. Hence, the author has to select an appropriate mesh size that gives good fidelity but with reasonable run times. For this study, the author uses square elements of 0.5 mm or two elements per mm in his simulations.

In the simulations to replicate the impact experiments, the author uses cylindrical projectiles made of A2 steel rods and heat-treated to a hardness of 55-58 HRC (The hardness value of HRC 55 is equivalent to material yield strength of 1.8 GPa). The projectile lengths range from ¾ in (~19mm) to 1 in (~25mm)

and the diameter is 0.297 in (~7.5mm). The author assigns a constant initial impact velocity to the cells covering the boundary of the projectile. For target plates, he sizes the models according to the actual experimental samples used with zero initial velocity constraint imposed. He places gauges at predetermined fixed points within the computation space and along the axis in both the projectile and target to measure dynamic properties such as pressure and material velocity. He then uses the output of these gauges to track the shock wave propagation and analyze the pressure attenuation characteristics in the target materials.

3. Material Models

An equation of state (EOS) is a fundamental thermodynamic relationship between pressure, specific volume, and specific internal energy. Since the focus of this study is on porous materials, the author will only discuss the porous P-α equation of the state compaction model option as used in AUTODYN® in detail. This actually consists of both a compaction model and an EOS for the solid material, and so it requires the user to specify several critical parameters that will describe the crush behavior of the porous material. The parameters are as follows:

a. Initial density of the porous material ρ_0
b. Bulk sound speed in the elastic compaction region
c. Maximum elastic pressure (pressure at yield) P_e
d. Solid compaction pressure P_s
e. Solid material Hugoniot parameters C and S.

The initial density of the porous material can be determined experimentally using the immersion density technique or more frequently, it is a parameter provided as a material specification by the material supplier.

The other input parameters for the computation model are determined using the methodology discussed in Grady and Winfree [13]. First, to determine the bulk sound speed, shown below is the relationship of how bulk sound speed c_e varies with initial density ρ_0 (3.1):

Bulk sound speed, $c_e = \sqrt{\kappa / \rho_0}$, where κ is the bulk modulus (3.1)

For isotropic materials, the bulk modulus κ is related to the Young's modulus, E, and Poisson's ratio ν by (3.2):

$$\text{Bulk modulus, } \kappa = \frac{E}{3(1-2\nu)} \tag{3.2}$$

Using the scaling relation (3.3) developed by Gibson and Ashby [3], [14], the expectation is for the Young's modulus E to vary with the square of density. The scaling relations for porous materials are derived mostly through empirical fitting of experimental data from extensive testing on polymeric foams.

$$\frac{E}{E_s} = \left(\frac{\rho_o}{\rho_s} \right)^2 \tag{3.3}$$

Assuming material isotropy during deformation, the bulk wave speed of the porous material can be related to the properties of the fully dense solid by (3.4):

$$\text{Bulk sound speed, } c_e = \sqrt{\frac{E_s \rho_o}{3(1-2\nu)\rho_s^2}} \tag{3.4}$$

In shock wave loading, the yield stress determines the Hugoniot elastic limit σ_{HEL}. Assuming linear elastic behavior to yield and a von Mises yield condition, σ_{HEL} can be determined from uniaxial stress loading yield strength σ_y by the relation defined in (3.5).

$$\sigma_{HEL} = \left(\frac{1-\upsilon}{1-2\upsilon} \right) \sigma_y \tag{3.5}$$

Using the σ_y data provided by the foam supplier, the author calculates the value of σ_{HE}. He then determines the maximum elastic pressure, P_e at which yielding initiates from the equation below as defined in (3.6). The Poisson ratio υ of the material comes from published literature and from supplier information [14], [15]. The hydrostatic pressure at which yielding occurs comes from Grady and Winfree [13]:

$$\text{Maximum elastic pressure, } P_e = \frac{1+\nu}{3(1-\nu)}\sigma_{HEL} \tag{3.6}$$

where σ_{HEL} is known to vary with foam initial density according to:

$$\sigma_{HEL} = C_y\left(\frac{\rho_0}{\rho_s}\right)^{3/2}\left(1+\left(\frac{\rho_0}{\rho_s}\right)^{1/2}\right) \tag{3.7}$$

This model, developed by Gibson and Ashby [14], predicts that σ_{HEL} increases with density as defined by (3.7).

The author calculates the values of σ_{HEL} for different foam densities of the same material using the σ_y data provided by the foam supplier. The constant C_y can then be determined from a least-squares fit.

Finally, to determine the pressure for complete compaction, P_s, the author uses the theoretical relation of σ_{HEL} as a function of density. The solid compaction pressure is therefore the elastic pressure P_e at which $\rho_0 = \rho_s$. He obtains the material properties required to compute the simulation inputs for the P-α compaction model from material specifications from the supplier (for FR-6700 rigid polyurethane foam) and Ashby et al. [14] for the aluminum metal foam. Figure 8 shows the P-α compaction model of FR-6720 polyurethane foam.

The solid material Hugoniot parameters, namely solid bulk sound speed, C and the Hugoniot shock velocity slope S, come from published literature [13].

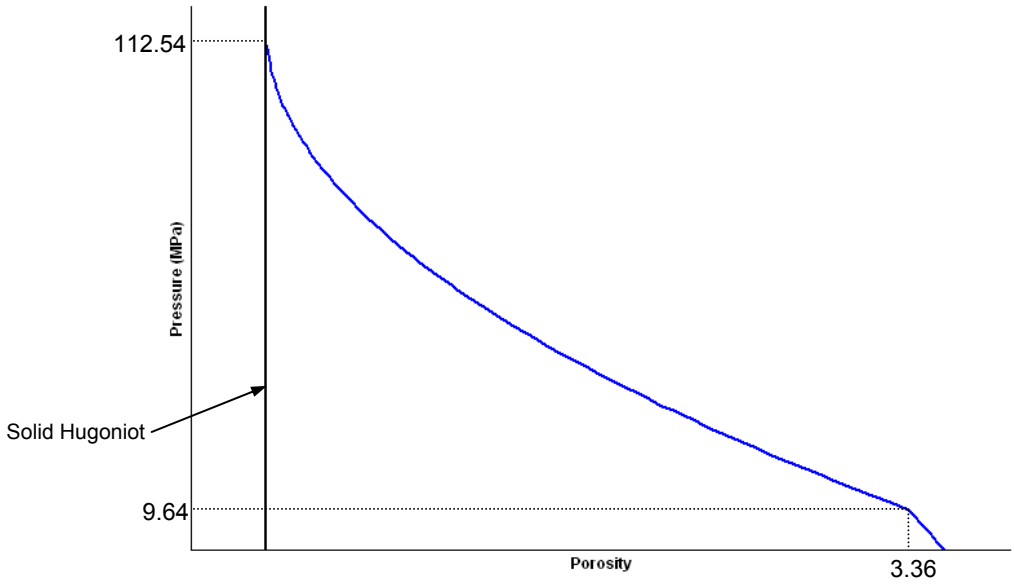

Figure 8. P-α Compaction Model of FR-6720 Polyurethane Foam

In order to completely describe porous material dynamic behavior, the author uses the P-α compaction model together with the von Mises yield strength criterion to model the strength effects. The von Mises yield criterion describes the material elastic limit and its transition to permanent plastic strain due to its inability to support large shear stresses. It is a simple criterion to apply, requiring only material shear modulus and yield strength inputs, and is conveniently applied when there is limited material strength information available. Material failure is modeled separately, and occurs when the material is not able to withstand tensile stresses exceeding the material's local tensile strength. The author uses the hydrodynamic tensile (P_{min}) model for these simulations, and the model requires a specified constant hydrodynamic tensile limit to determine failure occurrence.

The author has also chosen to use a commercially available polymeric fiber material, Dyneema®, with very unique properties as the wave-spreading layer in his armor concept. The Dyneema® material is made of several layers of ultra high molecular weight polyethylene (UHMWPE) fibers, with identical perpendicular fiber orientation in each layer. This orthogonal configuration allows for the distribution of the impact energy from the penetrator along the fibers much

faster and more efficiently than for an isotropic material. Dyneema® material is often used in the design of protective gear such as bulletproof vests. The orthotropic material model in AUTODYN® is commonly used to describe materials with different material properties or strengths in different orthogonal directions, and in this study, it will be used to describe the wave-spreading characteristics of Dyneema®. Assuming identical properties in the fiber directions, the author's chosen polymeric fiber material falls in a special class of orthotropic materials known as "traversely isotropic." As such, the longitudinal and shear sound speeds in the two fiber directions in the layer plane will be identical. The sound speeds in the fiber directions will also be much larger than the through-thickness sound speeds due to its anisotropy. This leads to higher elastic wave speeds and Young's modulii E_{22} and E_{33} in the fiber (or traverse) direction compared to Young's modulus E_{11} in the through-thickness (or longitudinal) direction. The thesis work of Ong discusses the Dyneema® orthotropic material model in detail [2].

The other materials in the armor concept use resident material models with modifications to known properties to match the actual material behavior, (for example, the Johnson-Holmquist 2 constitutive model for the ceramics). Figure 9 shows the material layering sequence for both the numerical and experimental studies. Table 1 summarizes the material properties used in the simulations.

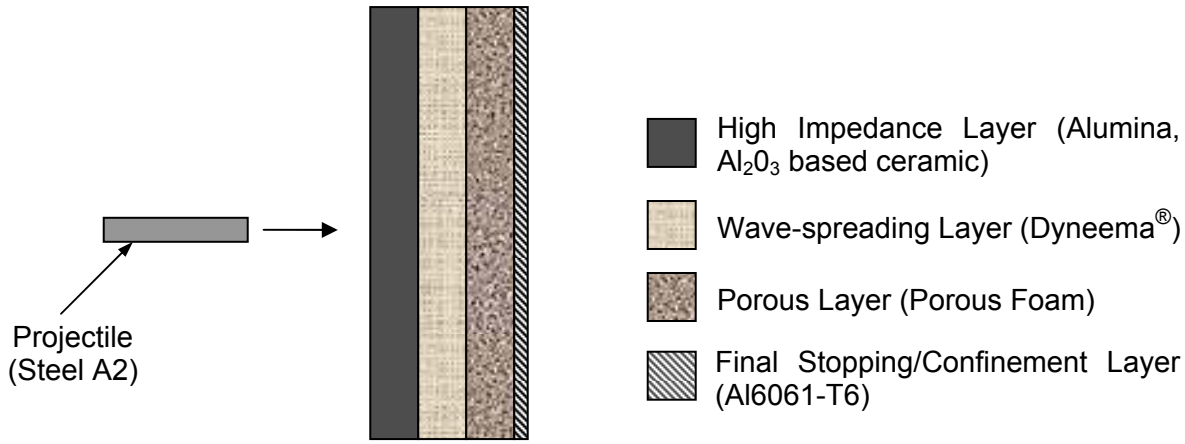

Figure 9. Material Layering Sequence for Simulations

Material	Equation of State	Constitutive Strength Model	Failure Model
Steel A2	Shock C = 4569 m/s S = 1.49	Johnson Cook G = 81.8 GPa σ_y = 1.8 GPa	Hydro (P_{min}) σ_{spall} = -2 GPa
Steel 4140	Linear κ = 159 GPa	Johnson Cook G = 77 GPa σ_y = 0.65 GPa	Johnson Cook D1= 0.05, D2= 3.44 D3=-2.12,D4= 0.002, D5 = 0.61
Ceramic Al203-99.5	Polynomial κ_{A1} = 231 GPa A2 = -160 GPa A3 = 2774 GPa	Johnson-Holmquist G = 152 GPa σ_{HEL} = 6.57 GPa	Johnson-Holmquist σ_{spall} = -0.262 GPa
Dyneema® D1n	Ortho E_{11} = 2.67 GPa E_{22} = E_{33} = 96 GPa ν_{12} = ν_{23} = 0.07 ν_{31} = 0.7 G_{12} = G_{31} = 1 GPa G_{23} = 36 GPa	Orthotropic Yield A_{11} = 1.5 A_{22} = A_{33} = 1 A_{13} = A_{13} = -0.68 A_{23} = 0.26 A_{44} = A_{55} = A_{66}= 4	Orthotropic Softening σ_{11}= 2MPa σ_{22}=σ_{33} = 2000 MPa τ_{12} = τ_{23} = τ_{31} =1.5 MPa E_{11}=5.447 KJ/m^2 E_{22} =E_{33} =0.3 KJ/m^2 E_{12} = E_{23}= E_{31} =14.613 KJ/ m^2
PR-6710	P-α P_{porous}=0.16 g/cm^3 P_e = 2.60 MPa P_s = 112.54 MPa C = 2490 m/s S = 1.56	von Mises G = 19.36 MPa σ_y = 2.60 MPa	Hydro (P_{min}) σ_{spall} = -2 GPa
Alulight®500	P-α P_{porous}=0.5 g/cm^3 P_e = 7 MPa P_s = 133 MPa C = 5240 m/s S = 1.40	von Mises G = 1.88 GPa σ_y = 7 MPa	Hydro (P_{min}) σ_{spall} = -2 GPa
Al6061-T6	Shock C1 = 5240 m/s S1 = 1.4	Steinburg Guinan G = 27.6 GPa σ_y = 0.29 GPa	Hydro (P_{min}) σ_{spall} = -2 GPa

Table 1. Material Properties for Numerical Simulation in AUTODYN®

C. CODE VALIDATION

1. Symmetric Impact: Tantalum-Tantalum Plate Impact

The author performs a simple plate-to-plate impact simulation to better understand the impact physics phenomena and to validate the AUTODYN® hydrocode. Both plates are of the same material, namely tantalum metal, because Hugoniot information for this material is readily available from the literature. Since this a simple problem that can be solved analytically, the derived solutions can then be compared to the simulation results. If the stress wave propagation characteristics are in agreement with analytical results, it will then give the author confidence that the simulation setup is correct.

The 2D symmetric impact simulation, performed using the Lagrange code solver, consists of a tantalum flyer plate that is 100 mm by 5 mm thick and a target plate of the same material that is 100 mm by 10 mm thick. The author uses a square grid meshing of two elements per mm and assigns a constant initial impact velocity of 500 m/s to the flyer plate. He uses gauges that are set up at an interval distance of 2 mm within the target plate to measure impact pressure as a function of propagation distance. Similarly, he places gauges at a 1 mm interval distance within the flyer plate along the axis of penetration (see Figure 10).

The simulated shock pressure profile indicated a peak impact pressure of 15.6 GPa at the first gauge location within the target (see Figure 11). The simulation results also revealed shock wave profiles that show flat top waves with short shock rise time (see Figure 12). The author observed a more gradual release with a decrease in pressure, as is expected for release fans. Using the momentum jump condition, material properties (see Table 2), and symmetric impact characteristic that the particle velocity u_p in the target is half the flyer initial velocity U_D, the impact pressure is analytically determined to be 15.5 GPa. The small difference in results and the small wave perturbations observed in the gauge pressure plots are due to numerical noise and artificial viscosity. The

usage of artificial viscosity hydrocodes allows the code to handle discontinuities such as shock waves where there are known issues with numerical instabilities. To model projectile penetration problems where shock waves are present, the natural viscosity of most materials is too small to damp out numerical instabilities caused by the very fast shock rise. Hence, artificial viscosity must be added to the pressure, which has the effect of spreading the shock wave over several mesh widths, and this transforms it from a discontinuity to a steep stress gradient and makes computation more manageable [12].

Upon collision between impactor (flyer) and target, a compression wave propagates into both the flyer and target with an initial pressure intensity of $P=\rho_0 U_s u_p$, where ρ_0 is the material density, U_s is the shock velocity (a characteristic of the material), and u_p is the particle velocity. Figures 11 and 12 show initial impact pressures of 15.6 GPa in both the flyer and target plate, which is consistent with the fundamental concept that if a discontinuity in pressure or particle velocity occurs across an interface, shock waves will be created to force the pressure and u_p to be equalized.

The analytical x-t and P-u_p diagrams (see Figure 13) also show material behavior under shock similar to the simulation results. For the x-t diagram, pressure and u_p are conserved across the impact surface at state 1. Since the flyer plate is thin in comparison to the target, the shock that was created at impact is reflected from the backside free surface of the flyer plate as a release wave, resulting in a complete release to zero pressure at state 2. This is similarly observed at 3 when the shock eventually reaches the free surface of the target plate at state 3. Negative pressure is then created at state 4 when the two release waves intersect, causing the target plate to see localized tension. If the dynamic tensile strength of the target material is exceeded, spall will occur, and the target plate will separate into two pieces. In Figure 12, it can be seen that at a time slightly greater than 4 μs the stress becomes negative. This corresponds to state 4 in the x-t diagram as discussed above, where the two release waves interact and cause tension.

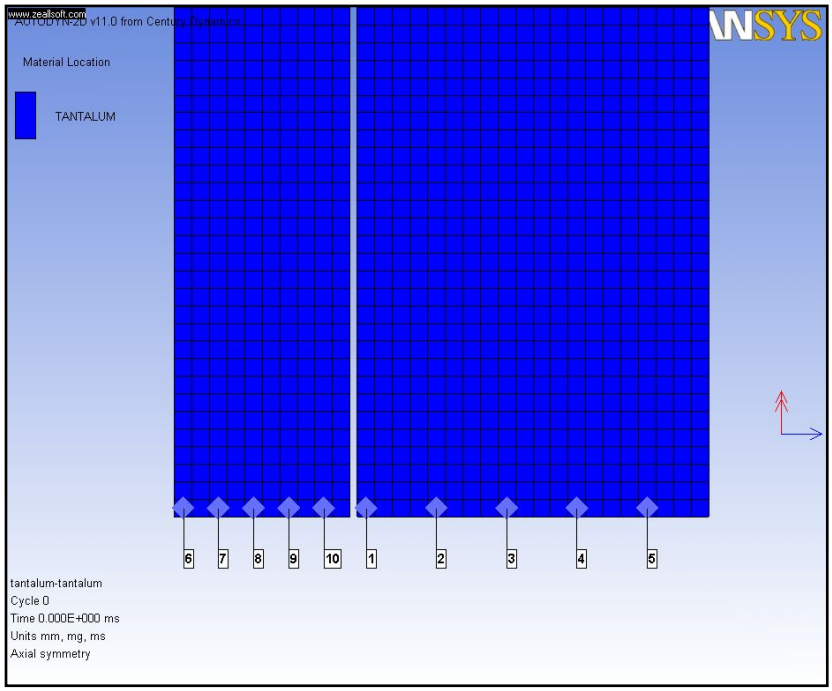

Figure 10. Simulation Setup for Tantalum-Tantalum Plate Impact

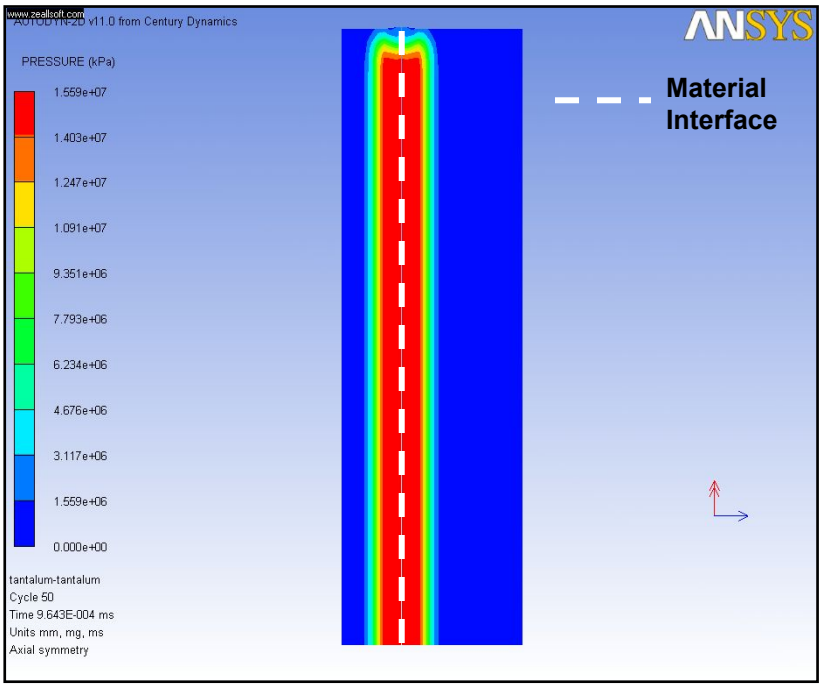

Figure 11. Shock Pressure Profile of Tantalum-Tantalum Plate Impact

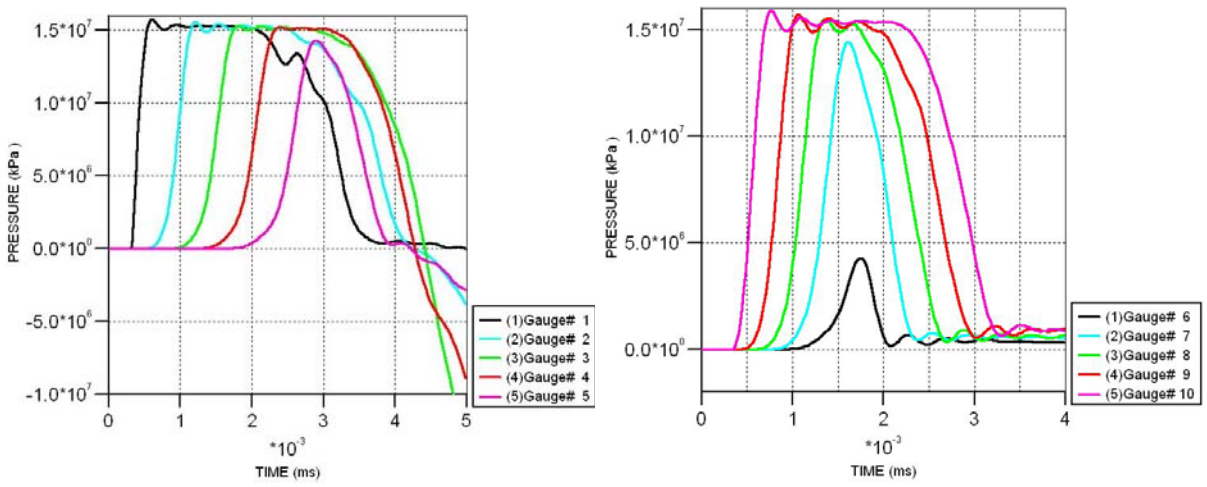

(a) (b)

Figure 12. Pressure versus Time Plot of (a) Target Plate; (b) Flyer Plate

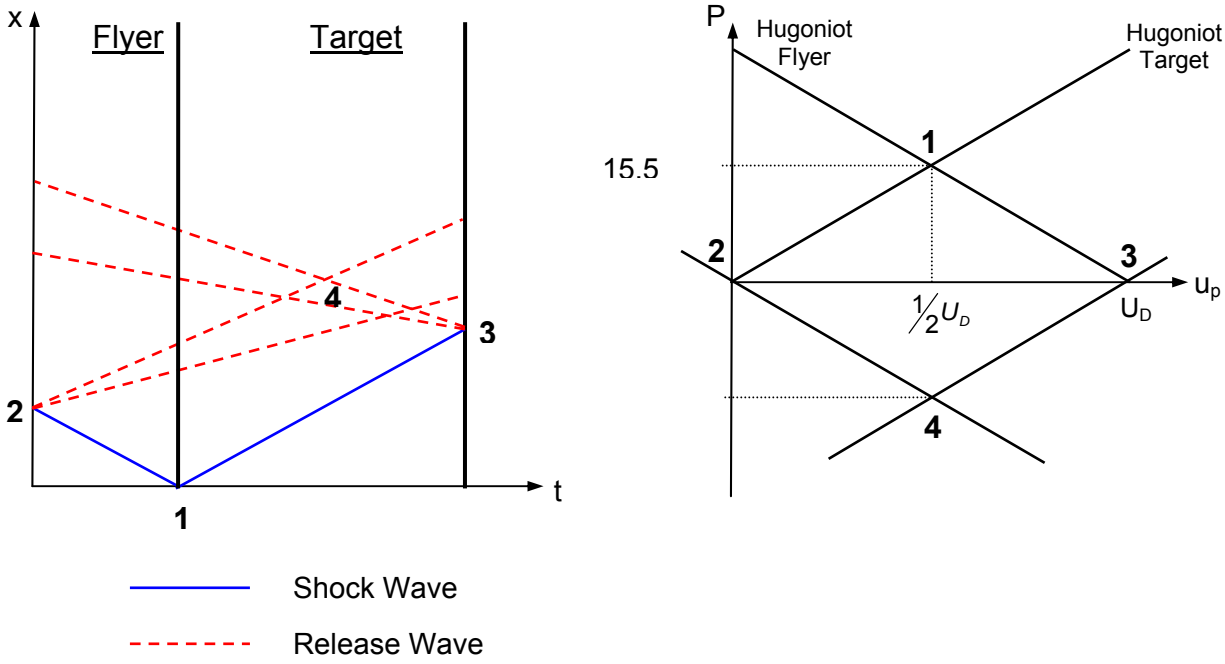

Figure 13. x-t and P-u_p Diagram for Symmetric Plate Impact

This negative pressure, or dynamic tension, is observed in the pressure wave profiles shown in Figure 12(a) for the target plate for several gauge locations.

To determine the linear U_s-u_p for tantalum, the author performed simulations using various initial impact velocities for the impactor. The impact pressure is then determined from the pressure plots, and by applying the momentum jump condition the shock velocity U_s is calculated. The linear U_s-u_p determined through simulations was found to be $U_s=1.38u_p+3.30$ (see Figure 14), which agrees reasonably well with the material properties of tantalum in Table 2. The author calculates this as a check to make sure the computer code is performing as expected.

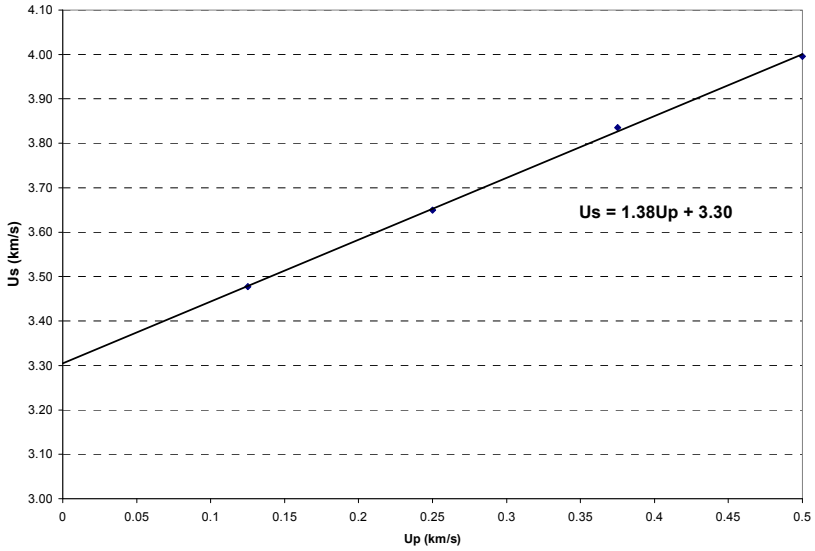

Figure 14. Linear U_s-u_p for Tantalum Metal

Since the simulation results are both qualitatively and quantitatively similar to analytical solutions, it gives the author confidence that the simulation setup accurately models the material behavior during impact.

2. Unsymmetrical Impact: Tungsten Projectile Impacting Tantalum Plate

To validate the simulation setup for an unsymmetrical projectile impact, the author impacted a rod-like tungsten projectile (4 mm in diameter) with constant velocity U_D of 500 m/s against a large flat tantalum target plate that is 100 mm x 100 mm by 15 mm thick. He used gauges that were set up at an interval distance of 2 mm within the target plate to measure impact pressure as a function of propagation distance. Similarly, he placed gauges at a 2 mm interval distance within the projectile along the axis of penetration (see Figure 15).

Upon impact, compressive shock waves propagated into both the target and the projectile, emanating from the interface. Figure 16 shows the edges of the planar waves in the target material being nibbled away within a short time due to lateral release waves from the free surface where contact with the projectile ceased. This happens in this geometry much more quickly than for the simulation above, which used a flyer plate of the same diameter as the target. These lateral release waves reduce the intensity of the compressive waves to form the spherical compressive pulse, and cause the initial state of uniaxial strain to become that of two-dimensional strain. During the simulation, the author observed compression of the ductile tantalum target plate in both the longitudinal and radial directions by the penetrating tungsten projectile. Since the lead shock is being relieved from the sides as it moves through the target, it quickly takes on a triangular wave profile. This occurs when release waves reach the shock front, and indicates that the shock is no longer supported from behind by the projectile. When the triangular compressive wave eventually reaches the back-free surface of the target plate, it is reflected from the free surface as a release (or tensile) wave. The negative pressure (see Figure 17) observed in the pressure profile in the tantalum target is the result of this wave reflection. This causes created tension within the target material. If the magnitude and duration of the tensile stress waves are sufficient, material failure, resulting in physical separation of the material in a variety of failure mechanisms can occur. For a ductile material like

tantalum, this failure is mainly due to ductile void growth, nucleation, and coalescence. The simulation results also confirmed that triangular shock waves are quickly obtained in the target, unlike the flat, top shock waves obtained for flat plate impacts, which results in their attenuation as they move through the target. This is expected as the small projectile experiences edge releases much faster compared to a large flat plate.

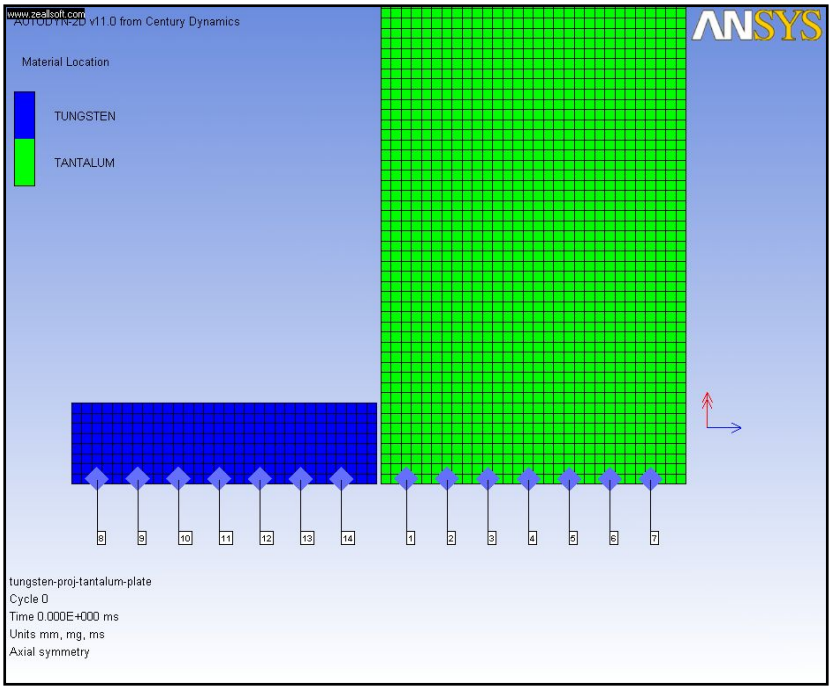

Figure 15. Simulation Setup for Tungsten Projectile Impacting Tantalum Plate

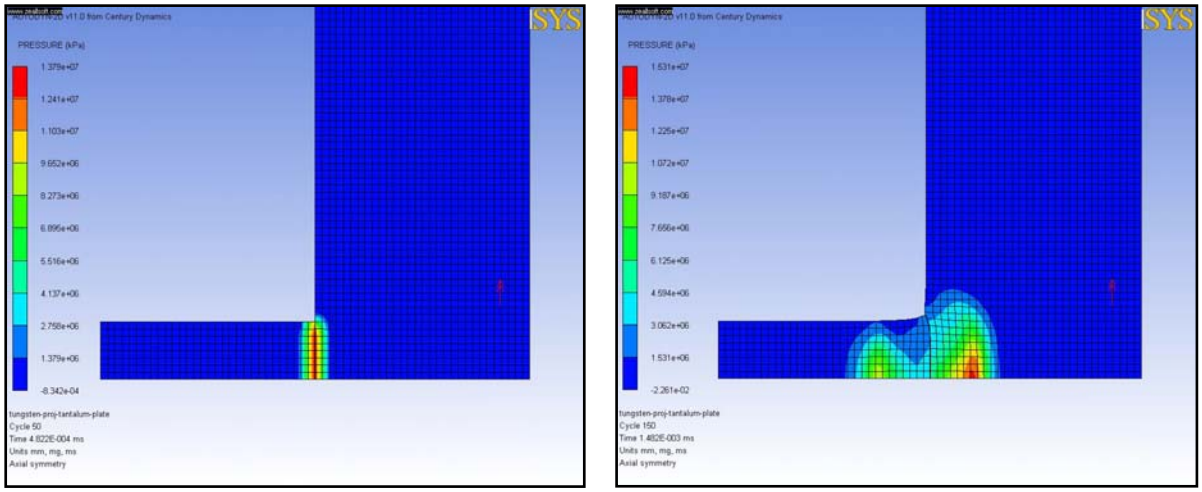

Figure 16. Pressure Plot at Initial Impact after (a) 0.5 μs; and (b) 1.5 μs

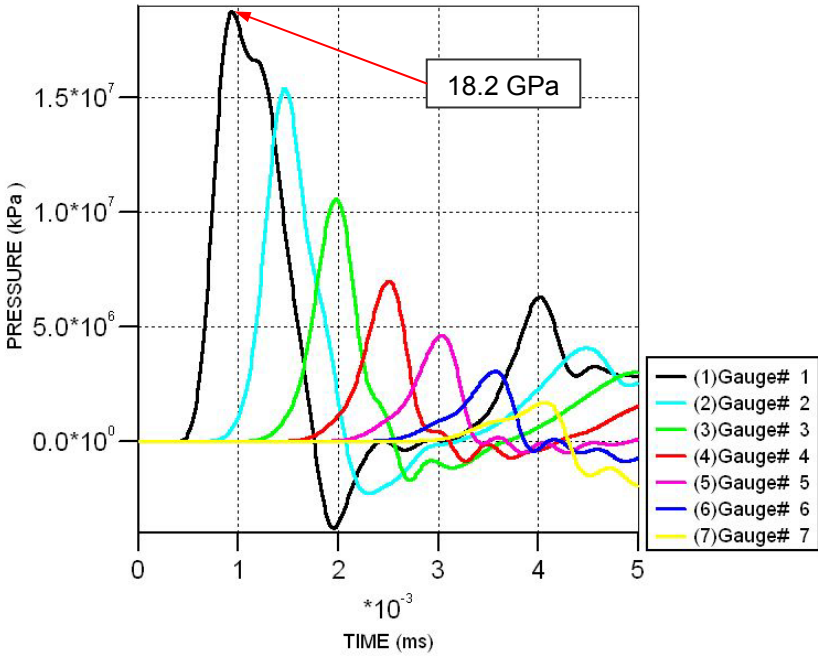

Figure 17. Pressure Versus Time Plot of Tantalum Target Plate

From the AUTODYN® simulation results, a peak pressure of 18.2 GPa was obtained. Using a technique known as impedance matching for unsymmetrical; impact, the peak pressure can be analytically determined by using the material properties from the AUTODYN® material library (see Table 2) and applying equal pressure and particle velocity boundary conditions at the interface.

Material	**Tungsten**
Density, ρ_{o1}	19.235 g/cm^3
Linear U_s-u_p relationship	$U_s = 4.04+1.23u_p$, where C_1= 4.04, S_1=1.23
Material	**Tantalum**
Density, ρ_{o1}	16.656 g/cm^3
Linear U_s-u_p relationship	$U_s = 3.43+1.19u_p$, where C_2= 3.43, S_2=1.19

Table 2. Material Properties from AUTODYN Material Library

By applying impedance matching, $P_1 = P_2$ (P_1: pressure in projectile; P_2: pressure in target plate) and

$(\rho_{01}S_1-\rho_{02}S_2)\, u_{P2}^2 - (2\rho_{01}S_1U_D+\rho_{01}C_1+\rho_{02}C_2)u_{P2} + \rho_{01}(S_1U_D^2 +C_1U_D) = 0$

Solving the quadratic equation derives $u_{P2} = 0.2844$ km/s.

Then, $P_2 = \rho_{02}(S_2u_{P2}+C_2)\, u_{P2}^2 = 17.85$ GPa.

Checking, $P_1 = \rho_{01}S_1(U_D-u_{P2})^2 + \rho_{01}C_1(U_D-u_{P2}) = 17.85$ GPa.

From the above, one can see that the simulation results agree reasonably well with the analytical results. Hence, it gives the author confidence that the simulation setup can accurately model unsymmetrical impact for a rod-like projectile impacting against a target plate.

3. Symmetric Impact: Porous Material (FR-6720 Polyurethane Foam)

Using the p-α material model as the author has defined it for the FR-6720 rigid polyurethane foam, he performed a simple symmetric impact simulation to investigate the material properties and wave propagation characteristics of the porous material. Two 100 mm square plates were generated using planar symmetry in AUTODYN®. The stationary target plate is 20 mm thick and the author assigned the 10 mm flyer plate an impact velocity of 500 m/s. Gauges are set up at an interval distance of 2 mm within both the flyer and target plate along the axis of penetration to measure the impact pressure (see Figure 18).

Figure 19 shows an initial impact pressure of 0.04 GPa, which is very low compared to the impact pressure experienced by a similar tantalum-tantalum impact simulation. The results also reveal that the porous material has good shock wave attenuating properties, which makes it suitable for energy absorption applications. However, due to its low density and hence poor resistance to penetration, it is not suitable as a first or second layer of a multi-layered composite armor structure. Hence, the author uses the porous layer as the energy absorbing third layer in his layered structure.

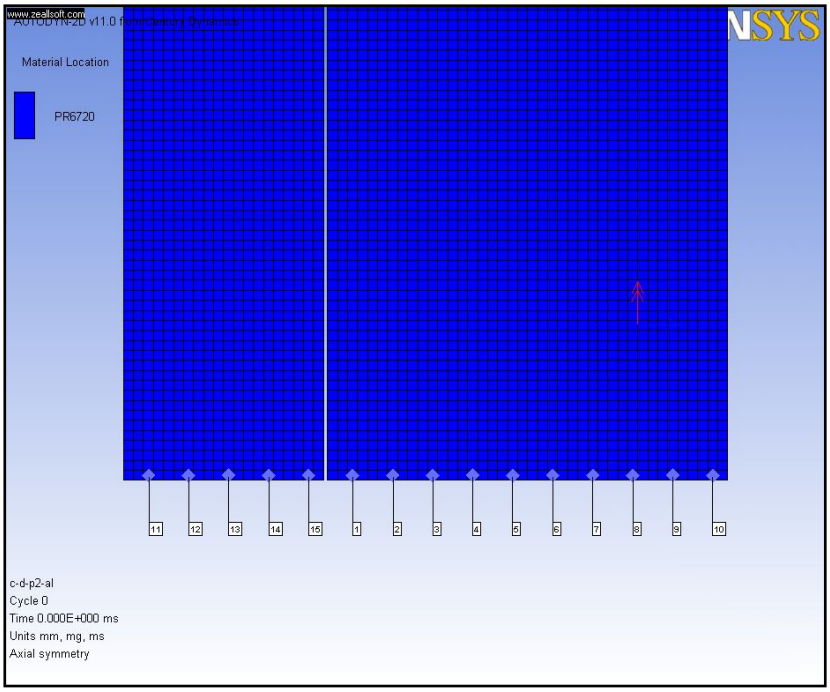

Figure 18. Simulation Setup for Porous FR-6720 Symmetric Impact

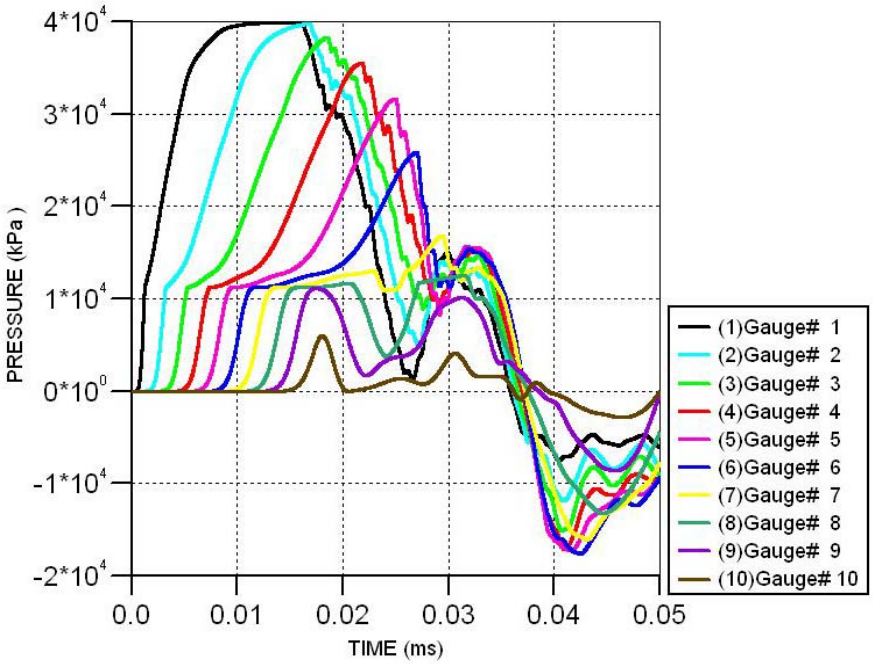

Figure 19. Pressure Versus Time Plot of FR-6720 Target Plate

Detailed analysis of the shock profile in Figure 19 revealed multiple shocks propagating within the porous target plate. The two-wave structure consists of an elastic wave, followed by a slower plastic wave. Figure 20 explains this wave propagation phenomenon.

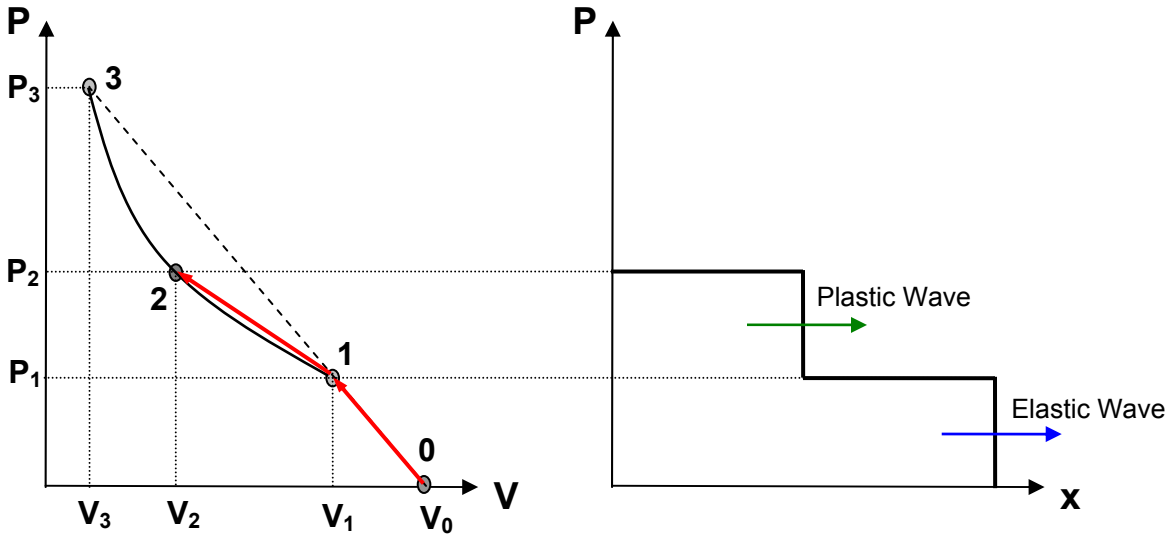

Figure 20. Elastic-plastic Transformation of Porous Material. After [7]

If the impact pressure does not exceed P_1 (the Hugoniot elastic limit σ_{HEL}), a single elastic wave will propagate in the material. However, if the magnitude of the applied stress exceeds σ_{HEL} but is not sufficient to reach state 3, two waves will propagate through the medium, the elastic wave and the plastic wave. The plastic wave moves with a speed that is a function of the slope of the Rayleigh line. It is noted that the σ_{HEL} value of 11.2 MPa from the pressure plot corresponds reasonably well with analytical σ_{HEL}=15.6 MPa, which is computed based on P_e =9.64 MPa for the porous FR-6720 polyurethane foam.

During the shock compression process from the initial rest condition at state 0 to state 2, the shock wave first drives the material to state 1, causing an elastic wave to form, followed by a second Rayleigh line to state 2, forming a slower plastic wave. Since the gradient of the Rayleigh line from state 1 to 2 is less than the Rayleigh line gradient from state 0 to 1, the plastic wave travels

more slowly than the elastic wave. From the pressure wave profiles in Figure 19, the elastic wave speed is found to be 1,100 m/s, which agrees reasonably well with the longitudinal wave speed of 1,022 m/s computed from the longitudinal modulus F of the material. The slower plastic wave speed is found to be 540 m/s from the pressure wave profiles.

If the impact pressure is increased to P_3, the elastic wave is overdriven and a single wave will propagate in the material. In this wave, yielding is still occurring but one cannot detect it from wave profiles because the plastic wave speed has exceeded the elastic wave speed. The effect of increasing impact pressure is demonstrated by increasing the impact velocity of the flyer. From the results shown in Figure 21, one can see that the plastic wave catches up with the elastic wave and will gradually disappear as impact velocity (or impact pressure) increases. A single wave will eventually form and this phenomenon can be verified through experiments.

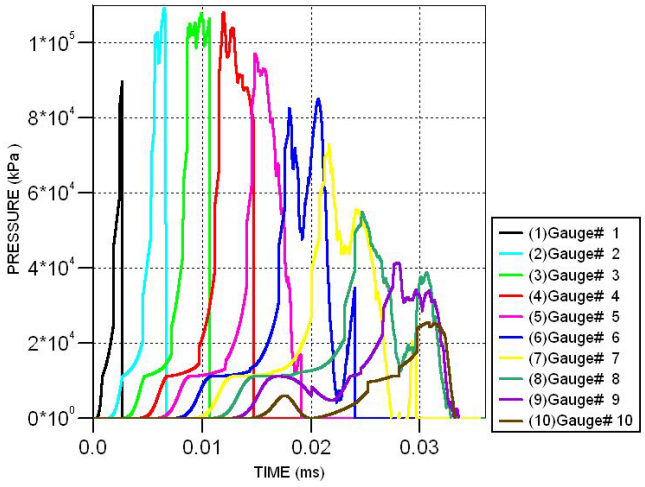

Figure 21. Plastic Waves Generated at Impact Velocity of 1,000 m/s

Since the above results showed credible shock wave characteristics and reasonable shock pressures, it gives the author confidence that porous material behavior has been modeled reasonably well using the P-α compaction model in AUTODYN®.

THIS PAGE INTENTIONALLY LEFT BLANK

IV. MATERIAL CHARACTERIZATION

Porous materials are characterized structurally by their cell topology (open cells, closed cells), relative density, cell size, and shape and cell size distribution [14]. This section describes the characteristics of the two foam materials studied in this research, namely the aluminum metal foam and rigid polyurethane foam, which the author used in two different initial densities.

A. ALUMINUM METAL FOAM

The aluminum porous material, supplied by Alulight® of America L.P., comes in the form of an aluminum foam sandwich. The aluminum foam sandwich (AFS) is a flat structure composed of a closed-cell, foamed aluminum core, and aluminum cover sheets. The sandwich panel is formed by foaming a powder metallurgy-precursor between the metal cover sheets. The powder metallurgy process involves blending atomized aluminum alloy powder with titanium hydride (TiH_2) and compacting the mixture to form a precursor material. The compacted precursor is then placed inside a mold and heated to a temperature near the melting point of the aluminum alloy. The foaming agent decomposes when subjected to heat and gas bubbles that get trapped form within the compacted powder body. The expanding gas bubbles then create voids within the expanding molten metal and the mold is rapidly cooled to prevent collapse of the foam structure. During the expansion process, the liquid foam is also metallurgically bonded to the solid cover sheets. Upon solidification, the cellular metal foam structure is formed [16].

Prior to physical examination of the foam structure, specimens of size 20 mm x 20 mm were cut from the large panel of 500 mm x 500 mm of thickness 12 mm. The AFS consists of a 10 mm-thick foam metal core sandwiched by 1 mm thick aluminum cover sheets. To avoid damage to the examined foam surface, a slow-speed diamond cutter was used to cut the specimen to size. Figure 22 shows the close-up view of a typical specimen. Using an open-source image

analysis software, ImageJ, parameters such as mean pore area, equivalent pore diameter, area fraction, and pore size distribution were determined. Table 3 shows a summary of the material characteristics and Figure 23 shows the graphical representation of pore size distribution of the metal foam.

Material	Alulight®500
Foam type	Closed cell
Nominal density of foamed metal core (g/cm^3)	0.5
Relative density	0.185
Mean pore size (mm)	2.27
Maximum pore size (mm)	4.56
Minimum pore size (mm)	0.24
Estimated pore volume (%)	75

Table 3. Summary of Material Characteristics of Alulight®500 Metal Foam

Visual inspection of the metal foam sections revealed that the foam has non-uniform pore structure with variable pore size. These effects can be explained by the unequal heating rate during manufacturing which leads to variable pore size. Each cell/pore is separated from another cell by a thin wall of metal. The results showed that the pore diameter ranges from 0.24 to 4.56 mm with the majority of pores within a size range of 1 to 4 mm in diameter. The size and distribution of pores within metal foams are usually random. The computed pore volume fraction of 75% is also representative of a typical porosity level of 70-90% for powder-metallurgy metal foams [17].

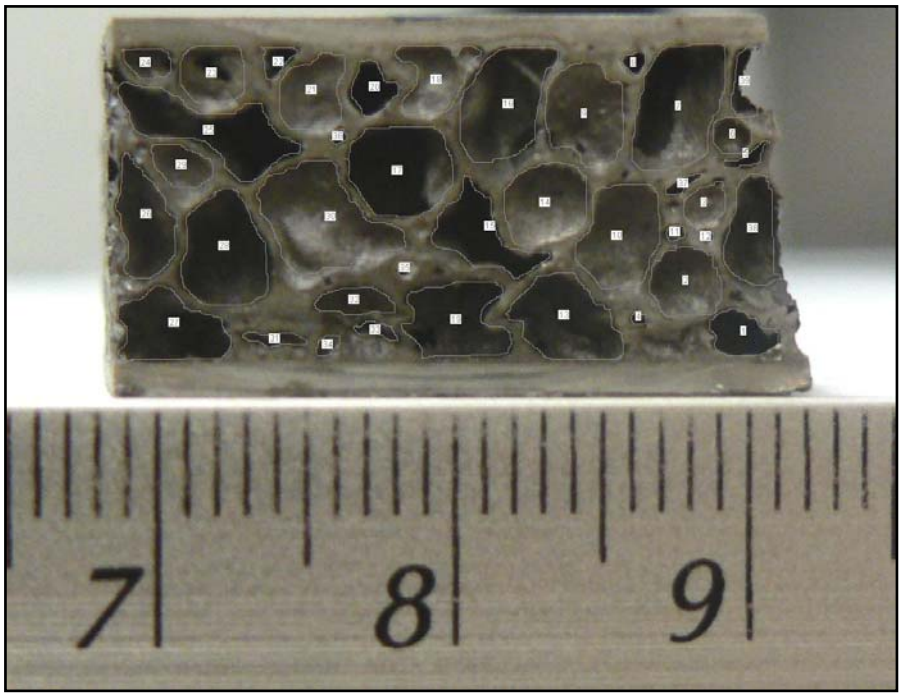

Figure 22. Close-up View of Typical Alulight® AFS Specimen

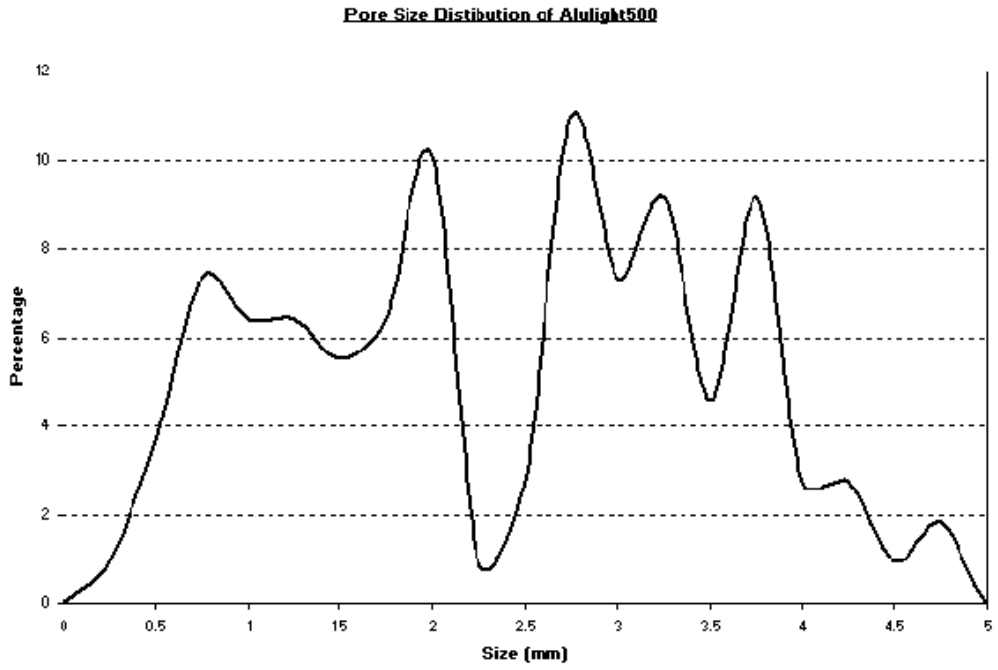

Figure 23. Pore Size Distribution of ALULIGHT®500 Metal Foam

B. RIGID POLYURETHANE FOAM

The rigid polyurethane foam, supplied by General Plastics Mfg Co., comes in sheet form 5 mm in thickness. Rigid polyurethane (PU) foams are commonly used in composite constructions, particularly as honeycomb aircraft-interior panels because of their low weight and high temperature compressive strength properties. Polyurethane foams are usually manufactured by a continuous-extrusion process to form blocks that are then cut to make sheets. The FR-6700 rigid polyurethane foam is a closed-cell, flame retardant polyurethane foam available in densities ranging from 10 to 25 lbs/ft^3 (0.16 to 0.4 g/cm^3). In this study, the author only investigates two foam densities: FR-6710, 10 lbs/ft^3 (0.16 g/cm^3) and FR-6720, 20 lbs/ft^3 (0.32 g/cm^3),

Specimens of size 50 mm x 50 mm were cut and examined under an optical microscope. Figure 24 and Figure 26 show microscopic images of the FR-6710 and FR-6720 PU foam respectively. Using the same image analysis software, the author determined the microstructural parameters. Figure 25 and 27 show the graphical representation of pore size distribution of the PU foam. Table 4 summarizes the material characteristics of the PU foam.

Material	FR-6710	FR-6720
Foam type	Closed cell	Closed cell
Nominal density (g/cm^3)	0.16	0.32
Relative density	0.126	0.253
Mean pore size (μm)	133.6	133.4
Maximum pore size (μm)	266.9	243.8
Minimum pore size (μm)	63.4	59.8
Estimated pore volume (%)	38	22

Table 4. Summary of Material Characteristics of Polyurethane Foams

Microscopic examination of the polyurethane foams revealed that the foam has variable spherical pores with diameters ranging from 50 to 300 μm. Both foam densities exhibit similar characteristics of mean pore diameter and pore size distribution, indicating that the foam manufacturing process is likely to be identical. The author also observed that the pore volume of the lower density

foam FR-6710 is almost twice of that of the higher density foam. This correlates well with the nominal foam density values claimed by the supplier.

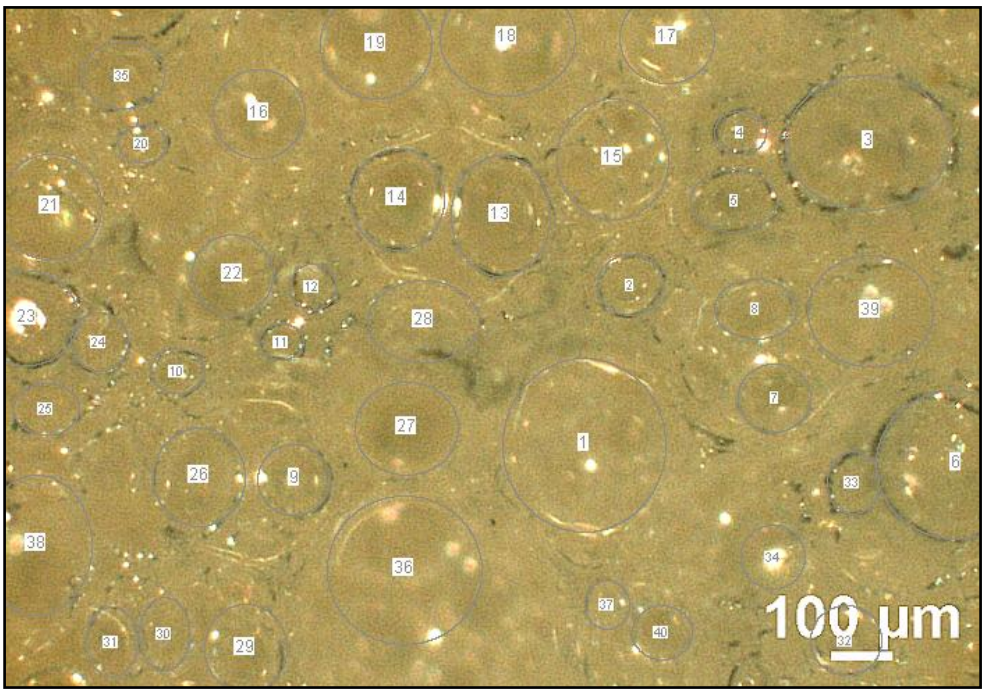

Figure 24. Microscopic Image of FR-6710 Polyurethane Foam

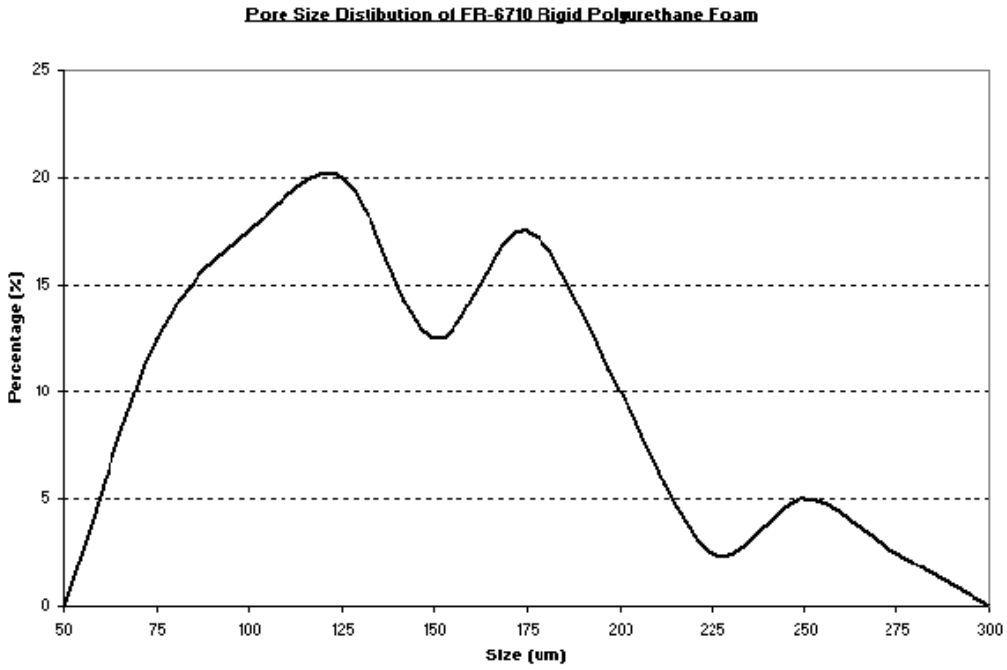

Figure 25. Pore Size Distribution of FR-6710 Polyurethane Foam

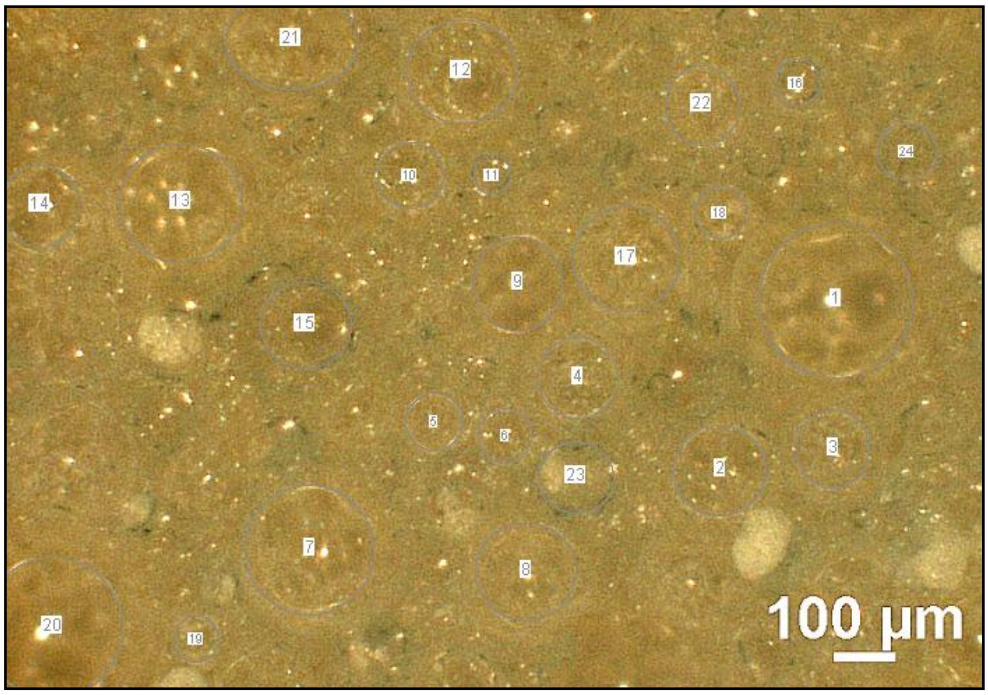

Figure 26. Microscopic Image of FR-6720 Polyurethane Foam

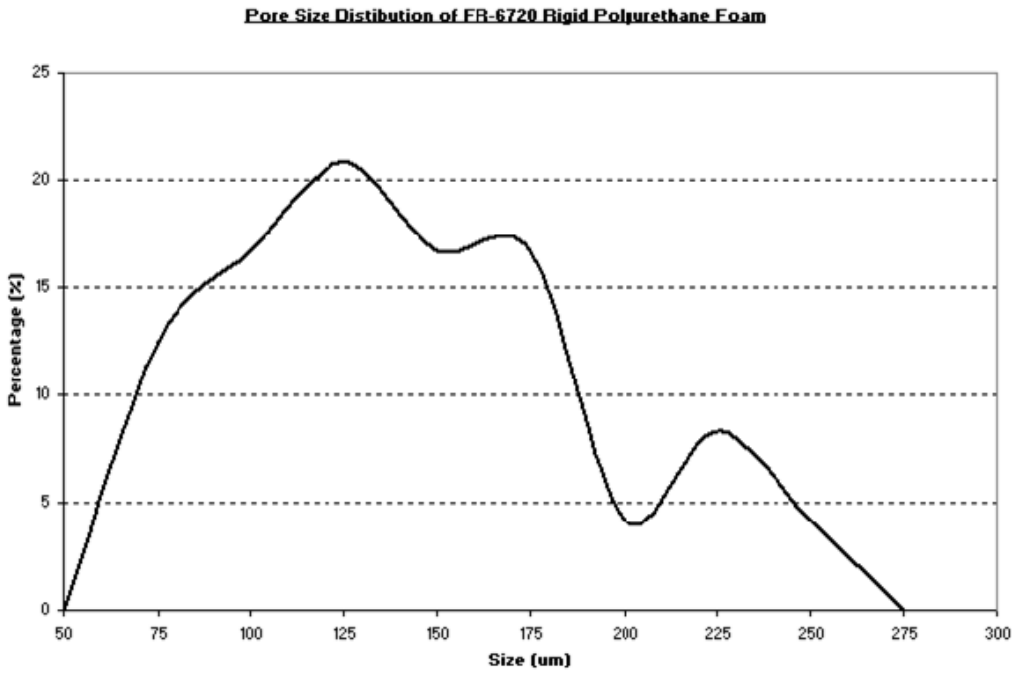

Figure 27. Pore Size Distribution of FR-6720 Polyurethane Foam

V. EXPERIMENT

A. INTRODUCTION

Since the focus of this research is to understand the effect of having a layer of porous material in an advanced layered armor concept, it is appropriate to do integral tests as a final validation. Since this layer is one of several, the author developed a test matrix for needed integral penetration experiments in close coordination with Ong [2], who has focused on the orthotropic material layer. Since the author was not able to measure the fundamental dynamic properties of the foam materials, he used literature values as input into the chosen material models used in the computer simulations. This allowed them to calculate the system response of each of the layered target geometries, and llowed for a close comparison with experimental results. In order to test the effectiveness of the porous materials, the author included what he believed to be appropriate tests with and without this layer. This section documents the experimental results.

B. TEST SAMPLE PREPARATION

The materials used to fabricate the layered structure were cut to the square test sample size of 100 mm by 100 mm. The mating surfaces were then cleaned thoroughly with alcohol to remove surface contamination. The materials were then bonded together using a low viscosity epoxy, AngstomBond 9110LV. This two-part adhesive exhibits good wetting, cures at room temperature, and develops strong, low-shrinkage bonds to most materials including glass ceramics, metal, and rigid plastics. The author selected a slow-curing and low-viscosity adhesive to minimize trapped air bubbles between the bond layers, which may affect the ballistic performance of the composite layered structure. After sufficient application of the adhesive to the mating surfaces, the author applied a controlled clamping force to the bonded layers to purge the excess

adhesive so that a thin bond layer could be formed (see Figure 28). The adhesive was then allowed to cure for 24 hours under a constant applied load. Extra care was taken to ensure that the applied load did not crush the pores of the porous materials.

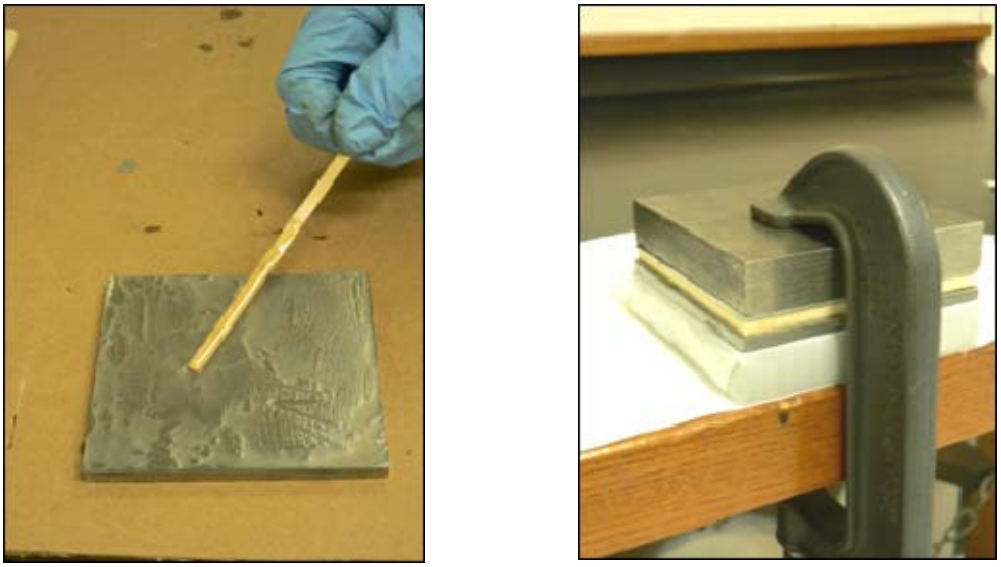

(a) (b)

Figure 28. Test Sample Preparation

C. EXPERIMENTAL SETUP

Impact experiments were conducted on a compressed-gas gun at the facilities of University of California, Santa Barbara (UCSB). With a maximum gas pressure of 2,000 psi, the maximum attainable projectile velocity for a 0.3" diameter steel rod of 1" length was found to be 484 m/s. Higher projectile velocities can be achieved by using smaller and lighter projectiles. Photographs of the experimental set-up are given in Figure 29.

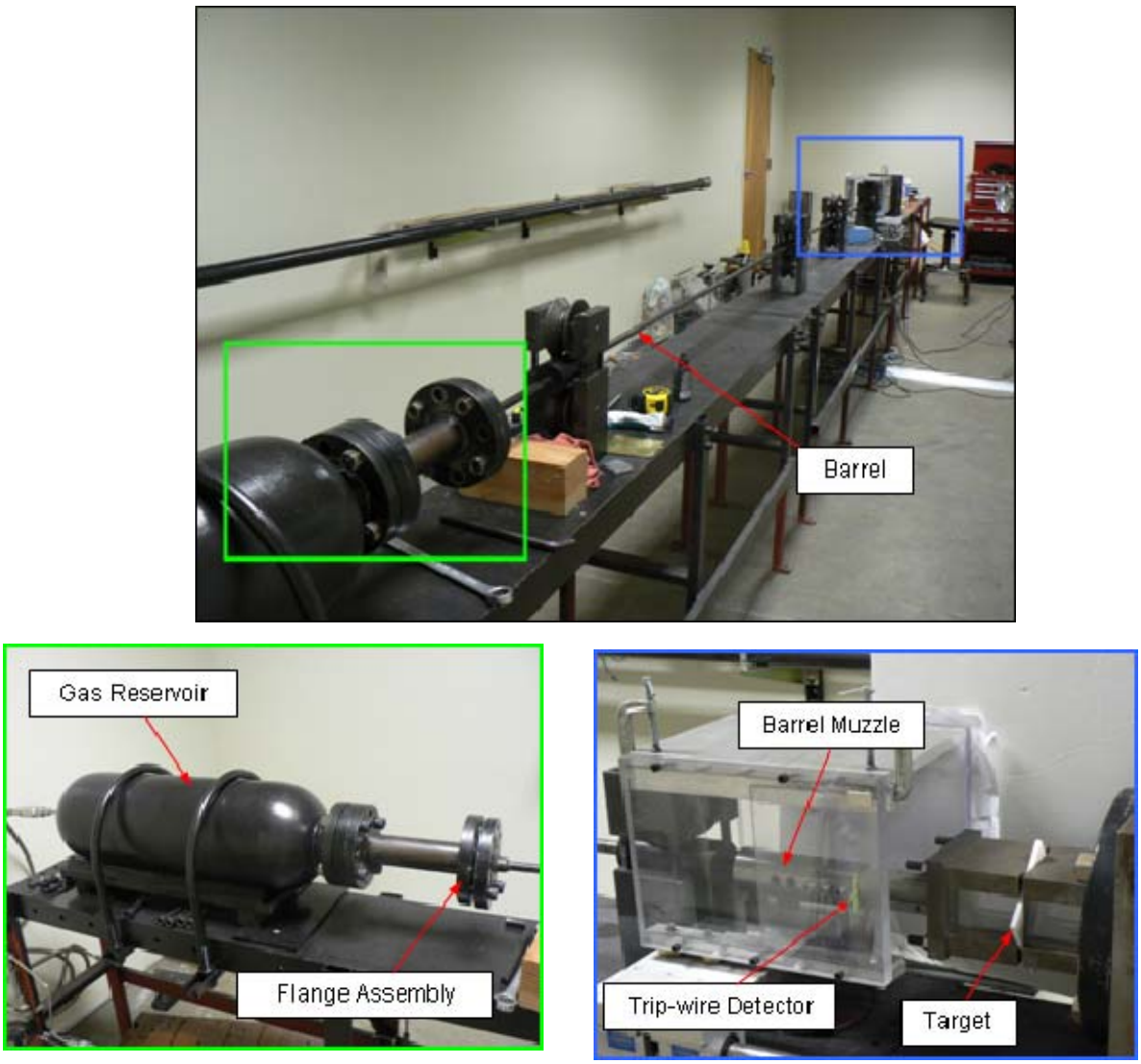

Figure 29. Photograph of Compressed-Gas Gun Facility

The gas reservoir and the barrel were connected via a flange assembly. The reservoir and the barrel could be separated by removing the securing bolts, and this enabled the projectile to be loaded into the 7.62 mm caliber smooth bore barrel. A steel diaphragm was then inserted between the flange interfaces before the flange assembly was re-assembled. When the reservoir was pressurized up to about 1,800 psi, the helium gas pressure ruptured the steel diaphragm and propelled the projectile towards the target, which was held in the impact chamber. The impact event was captured using a high-speed camera viewed through the transparent armor-glass in the impact chamber. The high-

speed camera used in these experiments to capture images at about 50,000 fps was triggered by a trip-wire detector that was placed at the exit of the barrel muzzle. Delays for the flash were calculated based on the expected projectile velocity. The projectile impact velocity was estimated using image analysis software to analyze the sequence of still picture frames captured by the high-speed camera. A projectile capture system using lightly compacted sand was placed behind the target in the event that the projectile penetrated the target.

D. EXPERIMENTAL RESULTS

Sixteen high-velocity impact tests with various experimental configurations were conducted at the gas-gun facility. As the focus of this study is on porous materials, only experimental data beneficial to this study are shown in Table 5. Other experimental data may be obtained from Ong [2]. Three types of porous materials were used in this investigation: rigid polyurethane foam FR-6710 and FR-6720 and Alulight®500 aluminum metal foam (in the form of AFS).

Shot No.	Test Sample	Areal Density (g/cm^2)	Projectile Description	Impact Velocity (m/s)	Complete Penetration (Y/N)
6	S	3.76	¾" Steel Cylindrical Rod	500	N
9	S-P2-Al	4.32	¾" Steel Cylindrical Rod	521	N
10	S-P2	3.92	¾" Steel Cylindrical Rod	509	N
11	S	3.76	1" Steel Cylindrical Rod	484	Y
12	C-D-M	3.87	1" Steel Cylindrical Rod	465	N
13	C-D-P2-Al	3.38	1" Steel Cylindrical Rod	465	N
14	C-D-P1-Al	3.30	1" Steel Cylindrical Rod	481	N
18	C-D	2.82	1" Steel Cylindrical Rod	483	N

Legend:

Symbol	Material	Thickness (mm)
Al	Al 6061-T6 Aluminum	1.5
C	Al 203-99.5 Ceramic	6
D	Dyneema	5
M	Alulight aluminum foam sandwich (AFS)	12
P1	FR-6710 rigid polyurethane foam	5
P2	FR-6720 rigid polyurethane foam	5
S	AISI4140 steel	4.76

Table 5. Summary of Experiment Results

The author performed a visual inspection of the post-impact samples and measured critical dimensions of the crater profile. Table 6 contains a summary of the post-impact test measurements on test samples. Figure 30 shows the schematic of a post-impact target plate with definitions of the measured parameters. During the ballistic testing, all laminates displayed attributes typical of armor under ballistic attack and will be discussed in detail in Chapter VI. However, it should be noted that the recovered steel projectiles showed brittle fracture failure upon impact. This is atypical of small-arms ball ammunition, which has a relatively soft steel core mass surrounded by a gliding jacket. The soft penetrating mass is made from 280HV soft steel, which enables it to deform when penetrating the target. Projectiles used for these tests shattered because they were made of hardened steel, and were therefore in a brittle condition. Therefore, the projectile that the author and Ong [2] used for these tests

exhibited minimal deformation and failed through brittle cracking rather than plastic deformation.

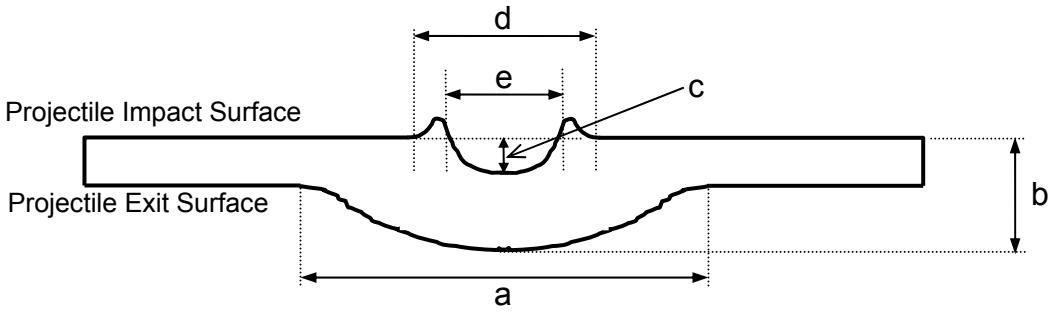

Figure 30. Schematic of Crater Profile Indicating Definitions of Measured Parameters

Shot No.	Test Sample	Bulge Width (mm)	Overall Depth (mm)	Max. Crater Depth (mm)	Max. Crater Base Diameter (mm)	Max. Crater Diameter (mm)
		a	b	c	D	e
6	S	19.88	12.01	2.26	13.83	9.15
9	S-P2-Al	72.94	15.81	4.94	13.54	9.61
10	S-P2	23.86	11.63	1.87	11.93	8.05
11	S	14.74	9.25	9.25	12.47	8.44
12	C-D-M	73.61	33.57	17.41	24.04	24.04
13	C-D-P2-Al	77.51	32.64	17.91	21.58	21.58
14	C-D-P1-Al	75.16	35.12	21.27	31.76	31.76
18	C-D	100	45.97	39.36	25.51	25.51

** All measurements made using digital vernier caliper*

Table 6. Summary of Post-impact Test Measurements on Test Samples

VI. DISCUSSION OF RESULTS

The author modeled the impact experiments using the numerical simulation setup discussed in Chapter III to match the actual measured experimental projectile impact velocity. He then compared the results of the analyses with actual experimental data. Upon validation of the models, the author will use AUTODYN® simulations to predict the performance of the various proposed multi-layered composite armor structures normalized to the same projectile velocity. The author performed the analyses to achieve the objectives stated below.

A. VALIDATE SIMULATION SETUP THROUGH EXPERIMENT

Figure 31 shows the results of shot number 6, which was a ¾" steel rod projectile impacting an AISI 4140 steel target plate at 500 m/s. The author placed pressure gauges at 1 mm and 4mm interval distances along the axis of penetration within the target plate and projectile respectively. When the projectile and target collided, very high pressures were generated in both the projectile and the target. For example, an impact pressure of about 9.5 GPa was attained in the target at the location of gauge 1. The wave profiles for gauges 1 and 2 have relatively flat tops, but subsequent gauges show triangular wave profiles. The triangular wave shapes are caused by release waves that are formed at the free surfaces. After 2μs, negative pressures are formed, indicating the presence of intersecting release waves. The intersecting release waves cause created tension within the target material, and if both magnitude and duration are sufficient, material failure may occur. Approximately 0.1 ms after impact, the projectile was stopped with a predicted overall penetration depth b of 12.5 mm. The localized plastic material deformation at the impact point observed in simulation predictions was similar to experimental observations. As compared with the experimental measurements for shot number 6 in Table 6 of the experimental results section, there is good agreement between the simulation

and experimental result. Simulation predicted that complete penetration would not occur and the author observed this experimentally. Figure 32 shows the post-impact condition of the target plate and high-speed photographs of the final moments of the impact sequence taken at 30μs inter-frame time.

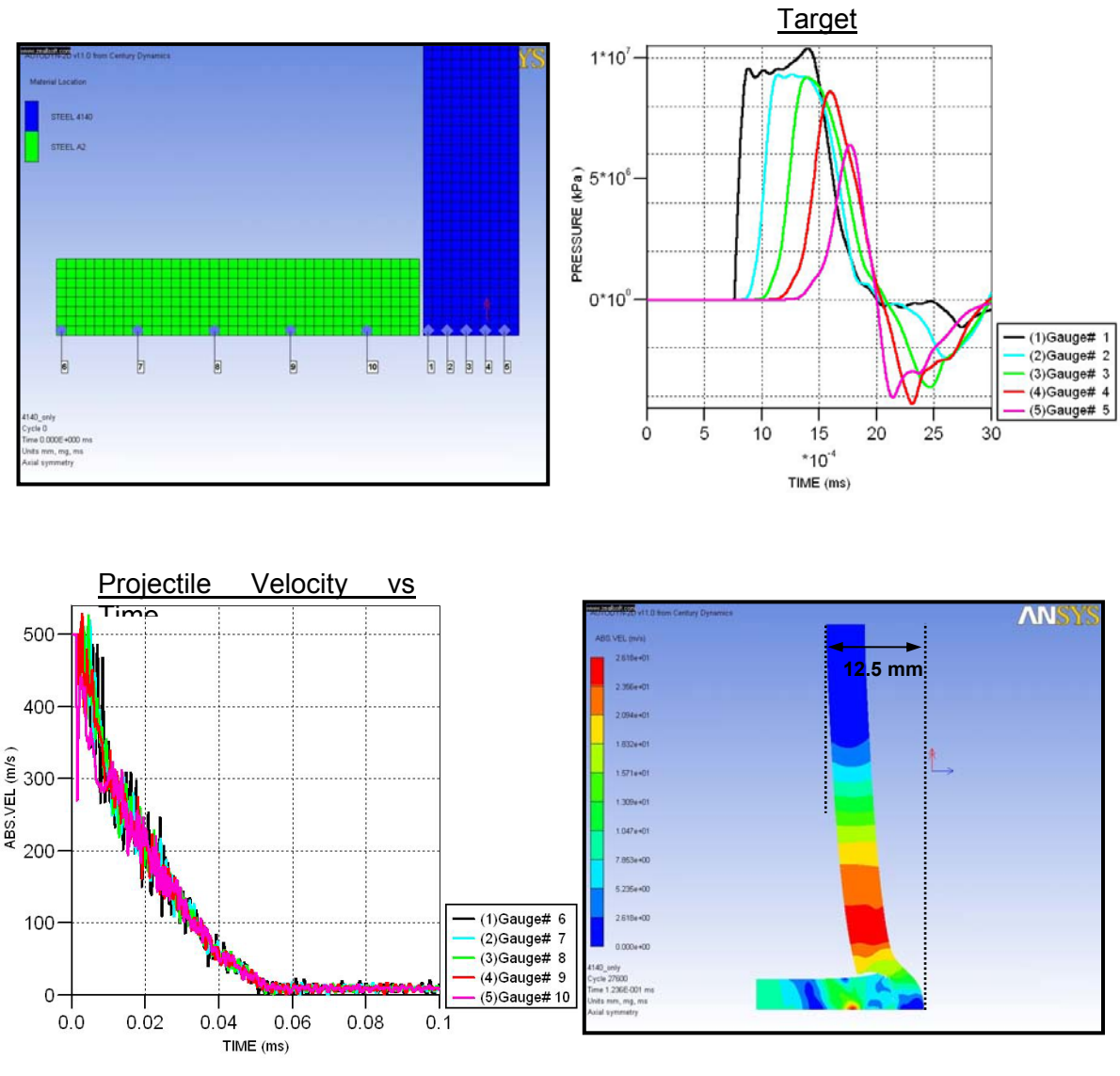

Figure 31. Simulation Results of Shot Number 6

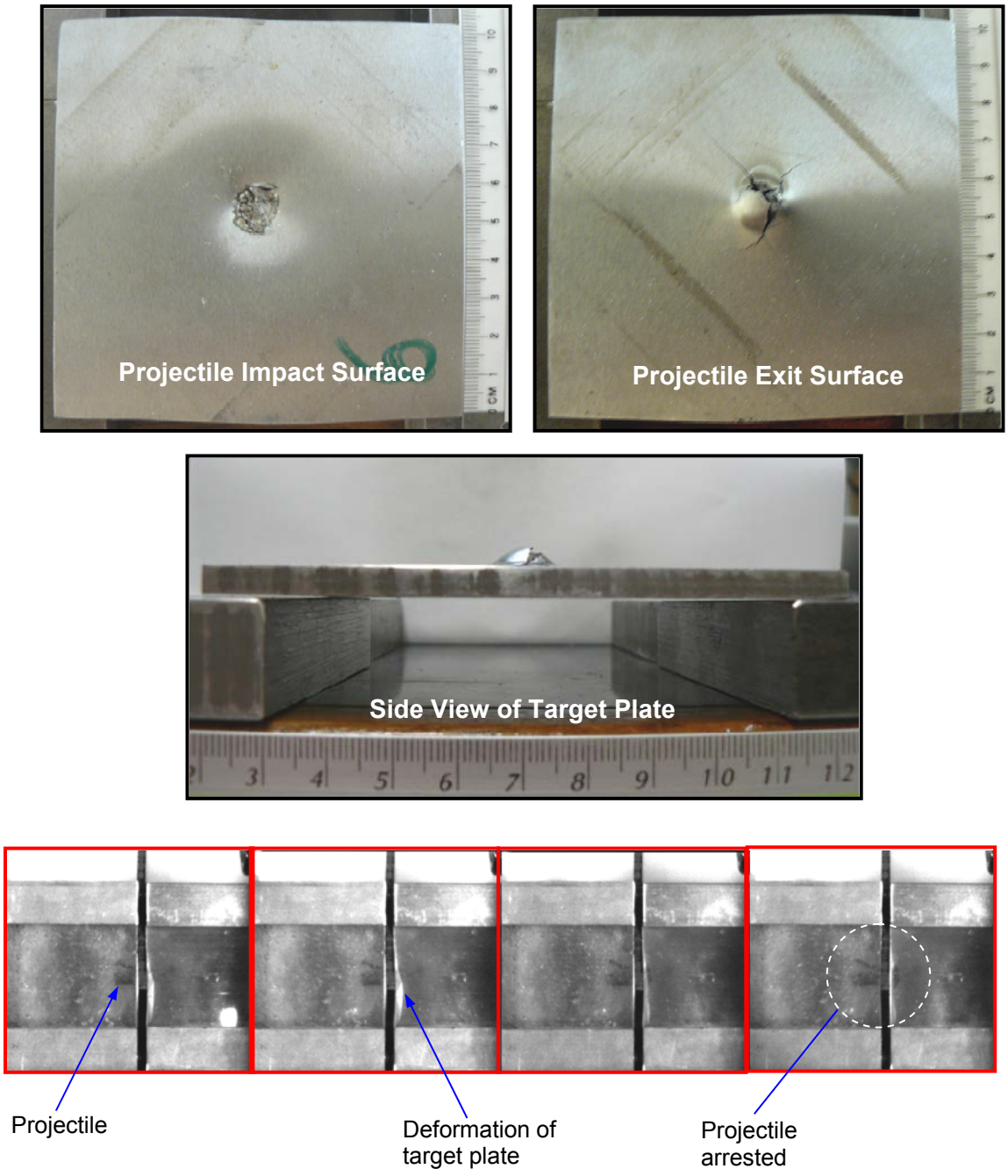

Figure 32. Experimental Results of Shot Number 6

Figure 33 shows the simulation results for Shot Number 11, which was a 1” Steel Rod projectile impacting an AISI 4140 steel target plate at 484 m/s. Figure 33 shows similar pressure wave profiles as in Figure 31, except with higher pressures. Figure 33 also shows that the 1” projectile actually perforates the steel plate with a residual velocity of 100 m/s at 170 μs after impact. Based on the velocity-time plot of the projectile, target perforation occurred at approximately 100 μs after impact. The author observed the occurrence of ductile hole growth with significant plastic deformation of the target material. The material is pushed out of the way of the projectile, revealing a through hole approximately the size of the diameter of the projectile. The simulation results agree well with the experiment for general observations and the final crater size. The high-speed photography showed brittle failure of the impacting projectile, leading to ejected debris with an estimated residual velocity of 118 m/s, which is in good agreement with the simulation results. The ballistic test results of Shot 11 also showed that the estimated kinetic energy required for penetration of the AISI 4140 steel plate is 1,000 joules. The author will use the ballistic performance of the AISI 4140 steel plate as a benchmark against the various multi-layered structure armor concepts he discusses in a later part of this chapter. Figure 34 shows the post-impact condition of the target plate and high-speed photographs of the final moments of the impact sequence taken at 30 μs inter-frame time.

From the above simulation results, the author concludes the validation of the simulation setup, projectile, and target steel material properties via the experiment results.

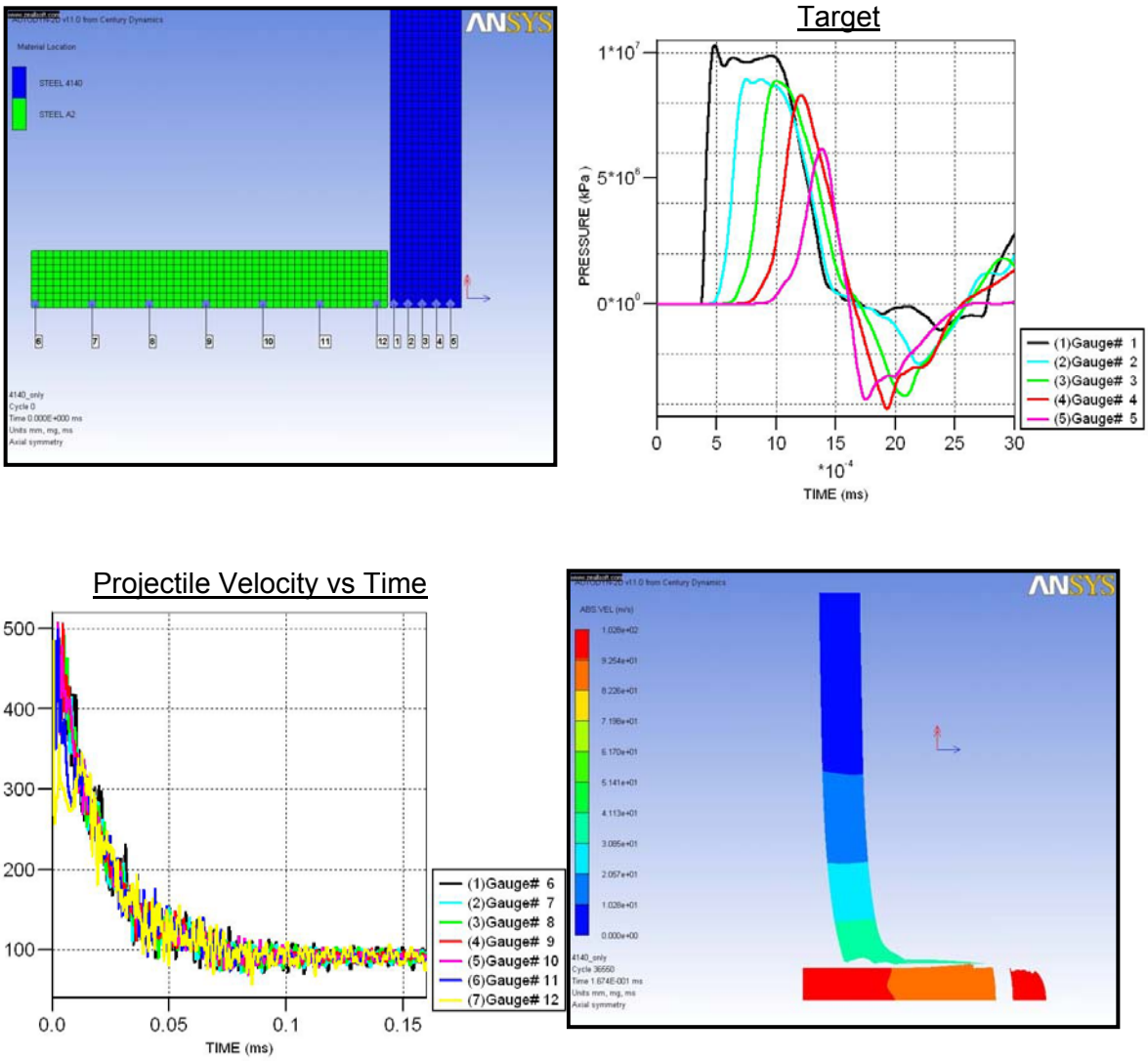

Figure 33. Simulation Setup of Shot Number 11

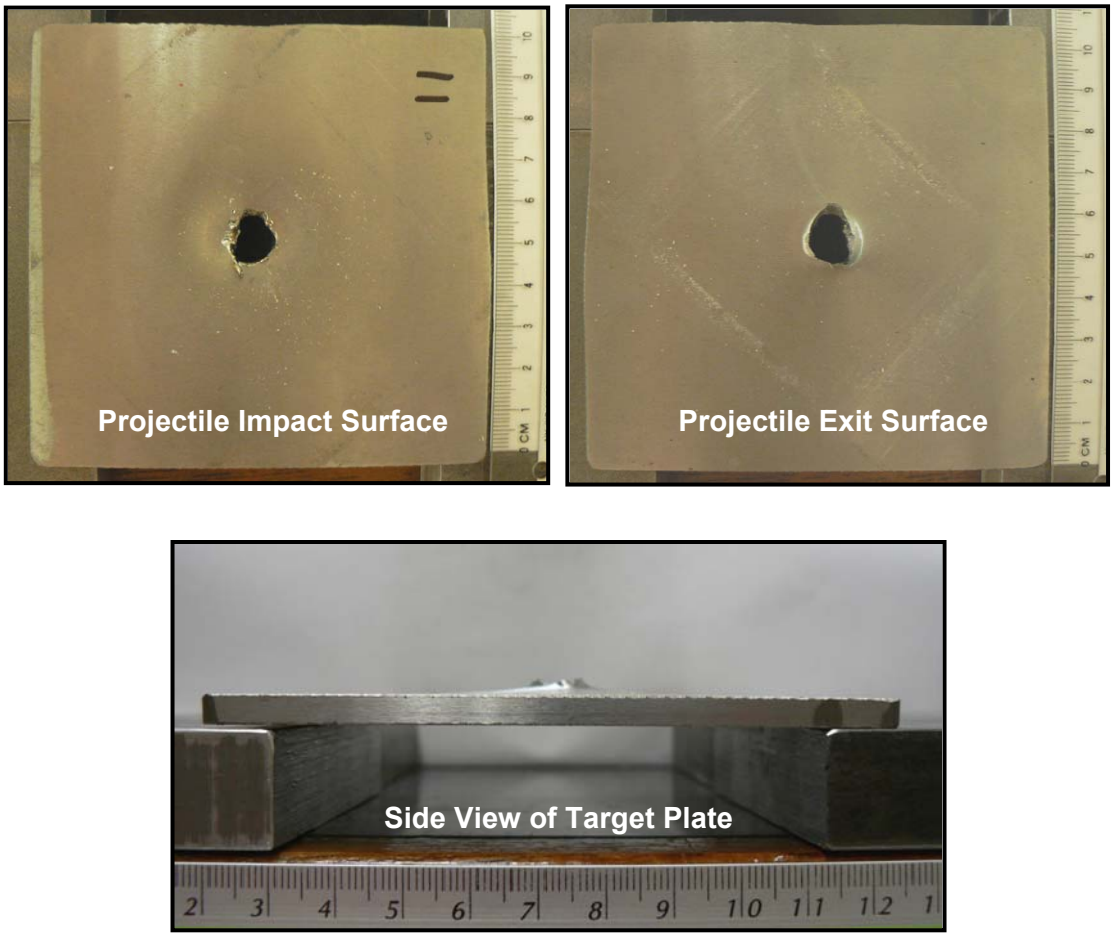

Figure 34. Experimental Results of Shot Number 11

B. ROLE OF INERTIAL BACKING PLATE

Figure 35 shows the simulation results of Shot Number 10, which was a 3/4" steel rod projectile impacting a S-P2 target plate at 509 m/s. In this experiment, the foam material *has no backing material*, and thus is unsupported. Figure 35 clearly shows that the compression shock wave is rapidly attenuated from 4.2 GPa at gauge 5 to 23 MPa at gauge 8 due to the shock attenuating properties of the porous material. This is equivalent to a pressure reduction of 99.5% across 2 mm of porous material. The pressure profiles in the porous layer also show the presence of a two-wave structure as explained in Chapter III.

Figure 36 shows the x-t diagram of the wave interactions. When the first shock reaches the foam material interface, the shock reflects off the interface as a release wave into the steel material and transmits into the porous material as a shock travelling at a lower shock speed. The shock speed in the porous material is lower than the shock speed in the steel plate because the foam material has a lower shock impedance and because this shock causes pore collapse. Since by this time the shock wave profile is triangular (unsupported), it attenuates as a function of run distance as the following release wave continuously erodes the shock front. The author also observed this effect in the steel material. When the transmitted shock arrives at the rear free surface, it reflects as a release wave, which further attenuates the peak shock pressure within the porous material. This explains the pressure wave attenuation recorded by the gauges in the simulation.

The simulation results also showed signs of spallation, which is consistent with observed experiment results. However, there was no complete penetration. Figure 37 shows the experimental results. Spallation is a process in which fragments of material are ejected from a body due to wave interactions that cause dynamic tensile state in the material [12]. Spall occurs when the dynamic tensile strength of the material is exceeded. Since there is a triangular wave shape, tension will be generated immediately upon reflection from the rear free

surface. The author does not expect this polyurethane foam material to have a very high dynamic tensile strength, so it will spall very easily as long as it sees tension. The author sees clear evidence for this process in the simulation, where material erosion is observed because of the spallation process.

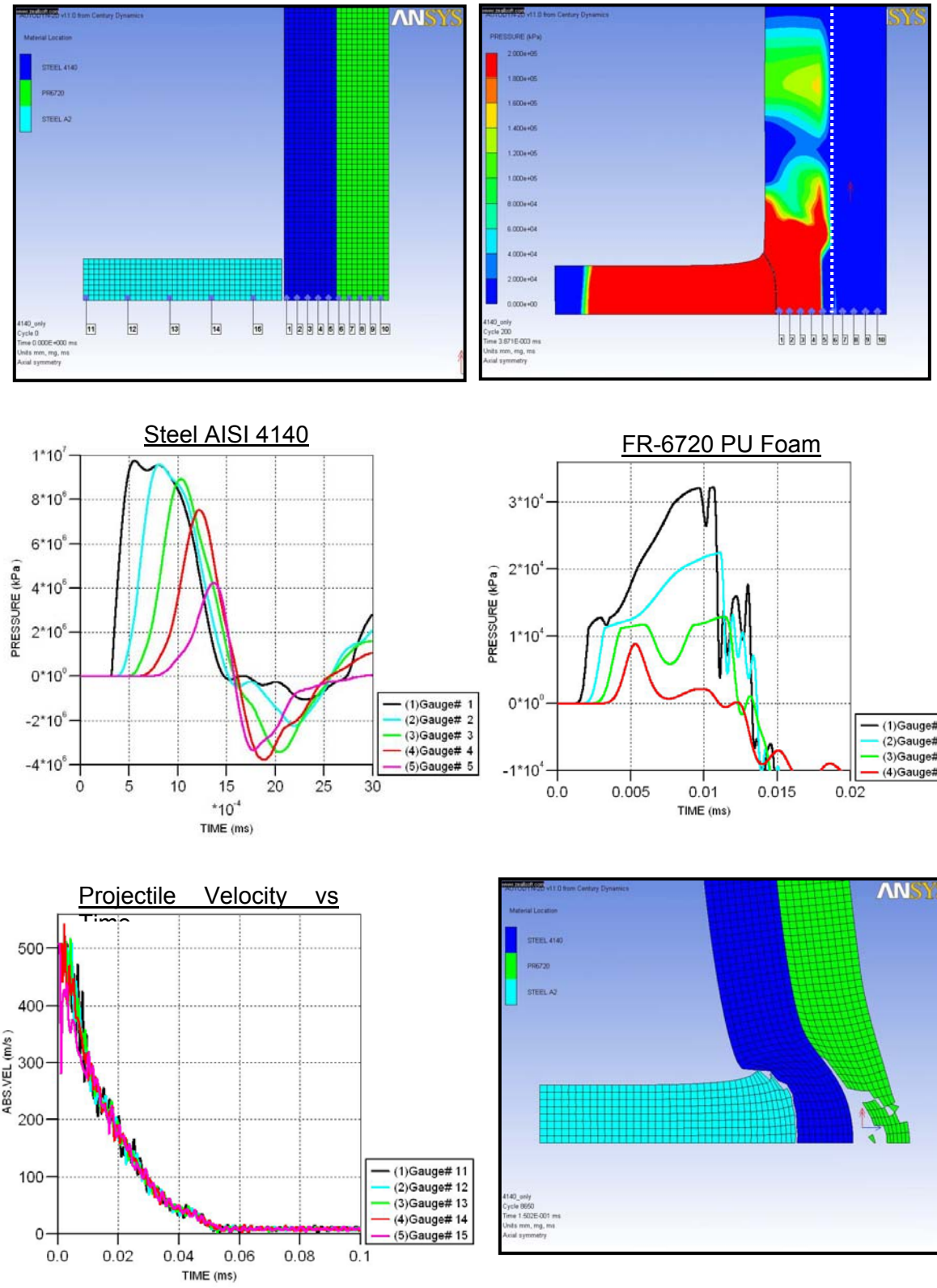

Figure 35. Simulation Setup for Shot Number 10

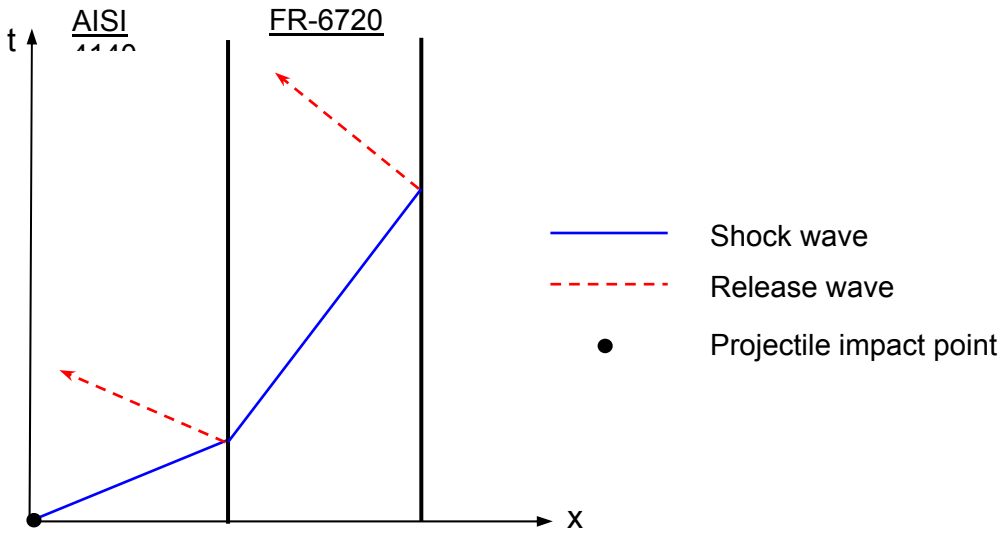

Figure 36. x-t Diagram for S-P2 Target Plate

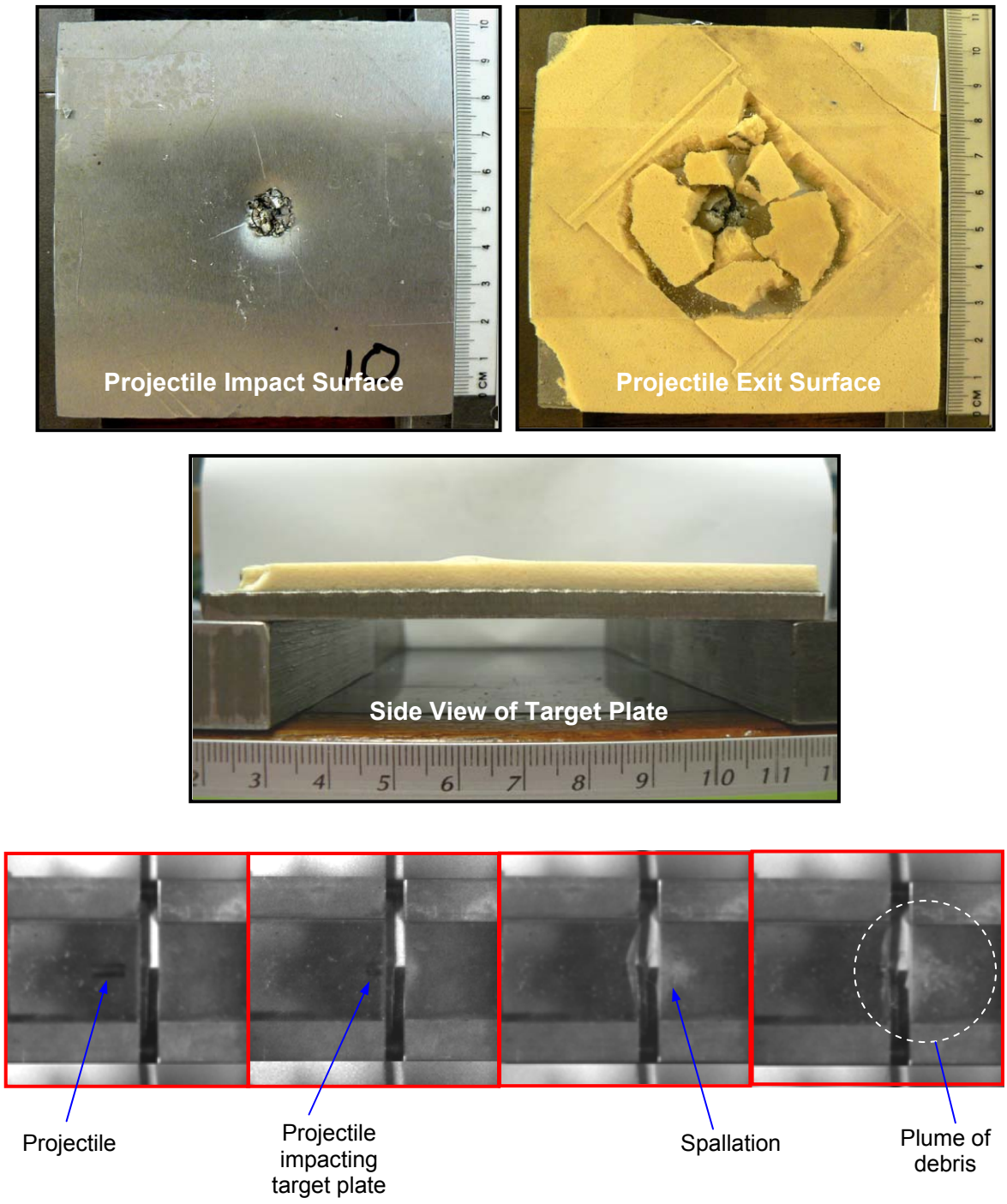

Figure 37. Experimental Results of Shot Number 10

Figure 38 shows the simulation results of Shot Number 9, which is a 3/4" steel rod projectile impacting a S-P2-Al target plate at 521 m/s. In this experiment, the author added a thin aluminum layer to the rear surface of the porous layer to provide support. Figure 39 shows that the porous material attenuates the compression pressure from 4.5 GPa at gauge 5 to 60 MPa at gauge 8. The pressure reduction is about 98.6% across 2 mm of the porous material. The x-t diagram in Figure 39 explains the higher peak pressures recorded by the gauges. The shock propagating in the porous material is reflected off the interface of the higher-impedance aluminum inertia backing plate as a re-shock, which then increases the gauge pressure. The simulation results show that the aluminum backing plate is plastically deformed due to the impact, but the porous rigid polyurethane foam is kept relatively intact. Complete penetration did not occur. The above results show good agreement between the code and the experiment. Figure 40 shows the post-impact condition of the target plate.

Comparing this result to that above for foam with no backing material, the author concludes that the inertial backing plate was necessary to constrain the porous material and prevent it from spalling. This then enables the porous media to perform its energy absorption role more effectively later.

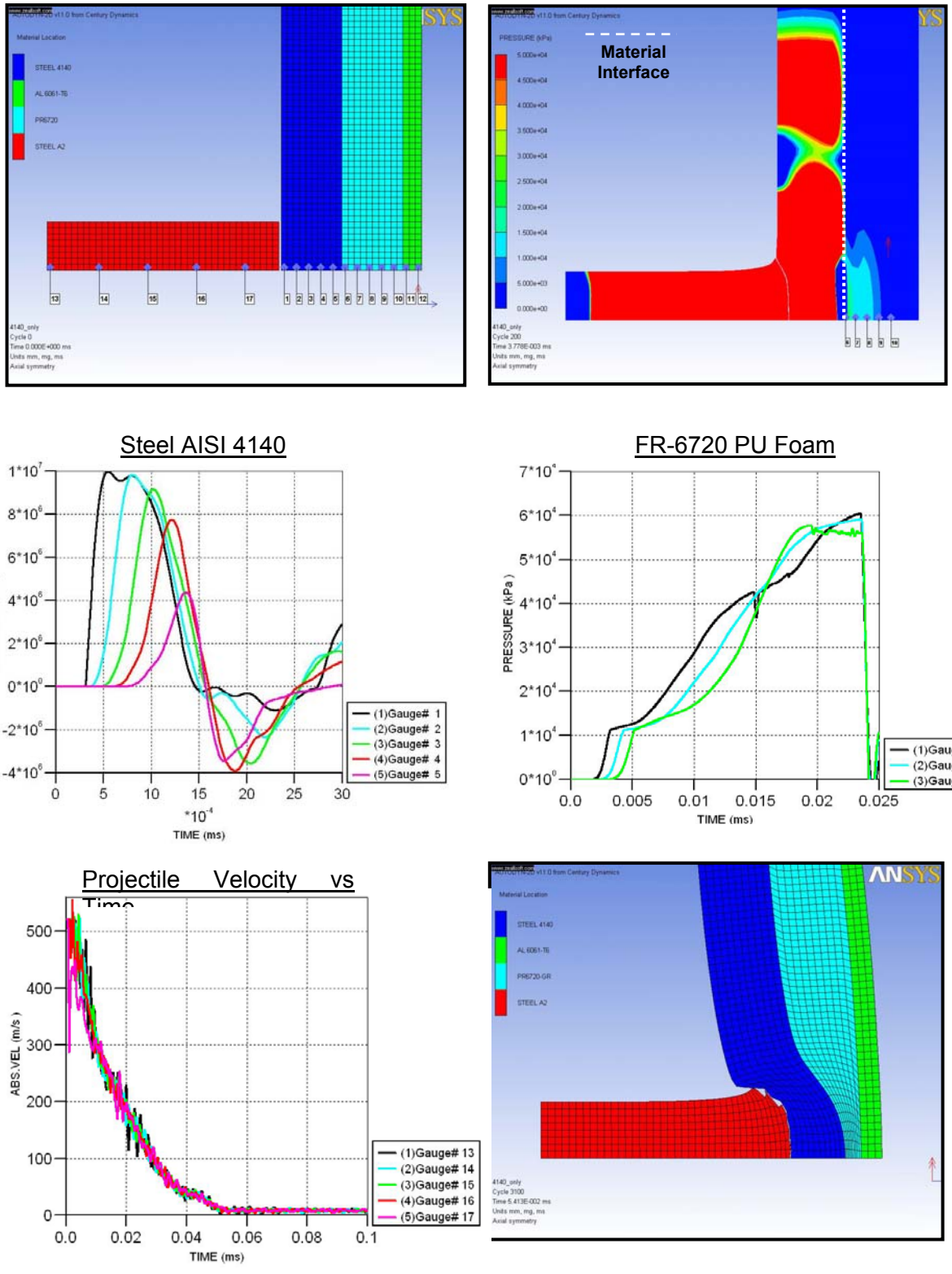

Figure 38. Simulation Setup for Shot Number 9

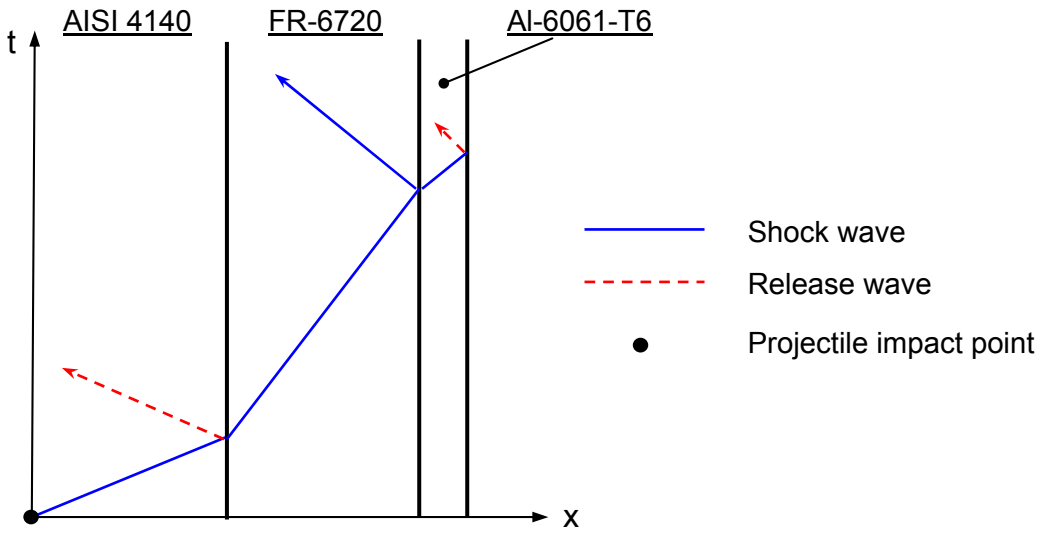

Figure 39. x-t Diagram for S-P2-Al Target Plate

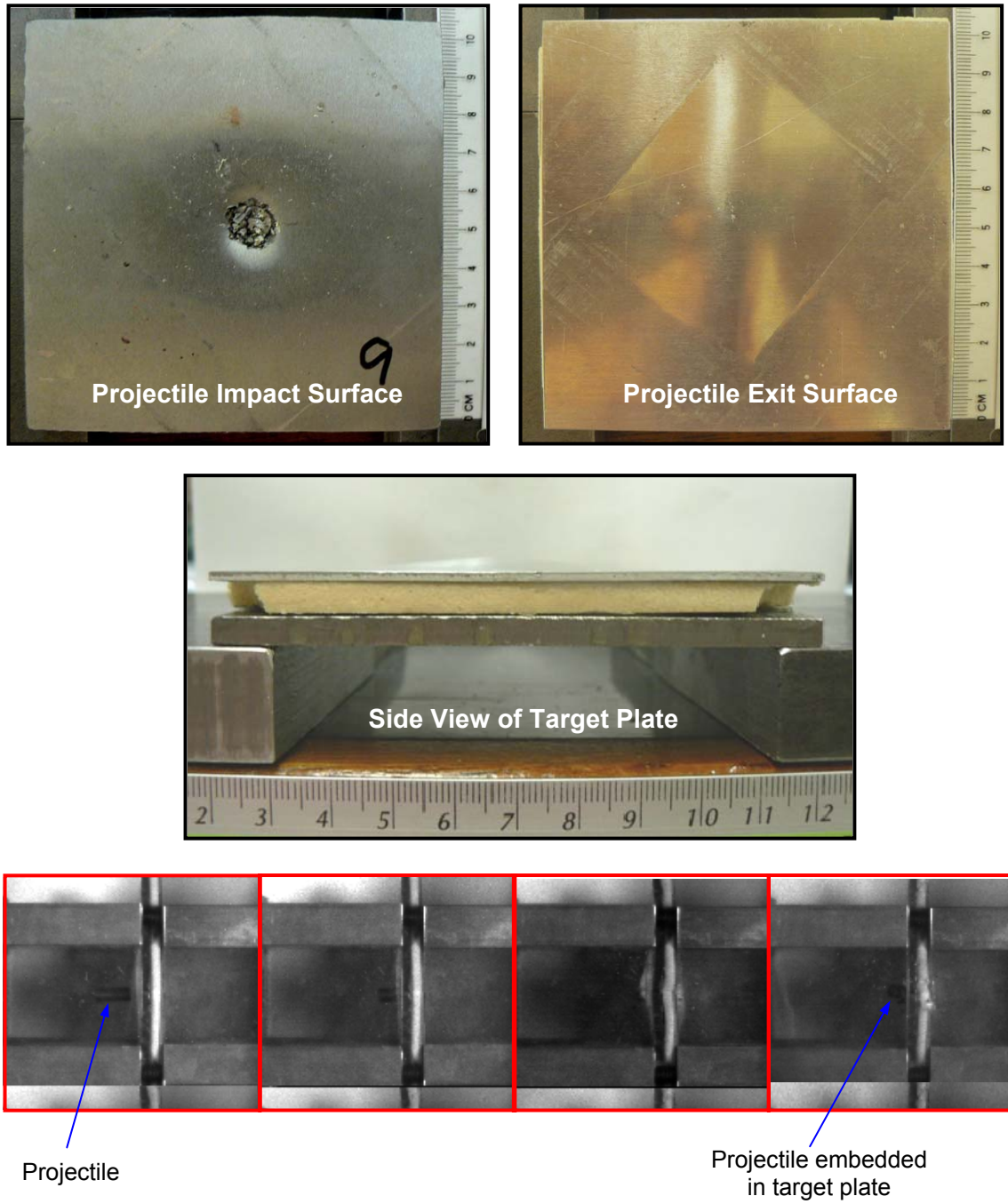

Figure 40. Experimental Results of Shot Number 9

C. MULTI-LAYERED ARMOR PLATE PERFORMANCE

There are several interdependent requirements such as cost, manufacturability, and structural and ballistic performance in the design of armor structures. While the overall design objective is to balance all these requirements, one usually uses a critical ballistic performance parameter such as dynamic deflection to control the design. Dynamic deflection is the maximum deflection the armor undergoes during a ballistic impact event. This distance is an indication of the standoff distance required to avoid physical trauma to the soldier wearing the personnel armor. For vehicle armor, the standoff distance affects the space available for loads and soldiers inside the vehicle. On one hand, large dynamic deflections are desirable since they generally result in improved ballistic efficiency, but they can lead to undesirable space requirements in standoff distance [18]. Since the focus of this current study is on the ballistic performance of the multi-layered armor concept, the author will use dynamic deflection as the performance metric.

As it was not possible to attain consistent projectile impact velocity for all impact tests, in order to conduct performance comparisons between different multi-layered armor structures the author has to first validate the material model parameters determined in Chapter III by performing AUTODYN® simulations to replicate the live firing experiments. Upon validation of the models, the author can then normalize the initial projectile impact velocities for the simulation models to the same impact velocity to allow a comparison study.

1. Ceramic-Dyneema® (C-D) Target Plate

The target plate consists of a 6 mm ceramic tile layered over a 5vmm Dyneema® material. Based on the recorded experimental data from Shot 18, the 1” length cylindrical A2 steel projectile impacted the composite plate at 483 m/s. Figure 41 shows the simulation results. The pressure profiles obtained from the impact simulation showed that the peak pressure is rapidly attenuated

by the wave-spreading properties of the Dyneema® material. The pressure plots also showed that the wave speed in the through-thickness direction is much smaller than the lateral wave speed, as expected for this material. The composite plate resisted complete penetration and the detainment of the projectile was about 0.32 ms after impact.

The role of the ceramic layer in an impact event is to deform the projectile and strongly dissipate its energy before it reaches the Dyneema® backing plate. This happens by causing extensive plastic deformation in the projectile, effectively turning kinetic energy into internal (heat) energy. Ceramic materials possess very high compressive strength but are very weak in tension. Hence, ceramics are extremely brittle and susceptible to fracture. Figure 42 shows the post-impact condition of the target plate. The ceramic layer showed heavy cracking because of the impact. Radial cracks propagated away from the impact point to the edge of the plate, and a large quantity of ceramic material had pulverized and ejected during the impact. The large deformation in the Dyneema® material resulted in layer delamination within the material and fiber stretching, both of which cause kinetic energy to be absorbed. The failure mechanism observed in the simulation agrees well with the experimental results. Furthermore, the overall deformation measurements are also comparable (see Table 7). Since the simulation results are both qualitatively and quantitatively similar to the experimental results, it gives the author confidence that there is accurate modeling of the material behaviors in AUTODYN®.

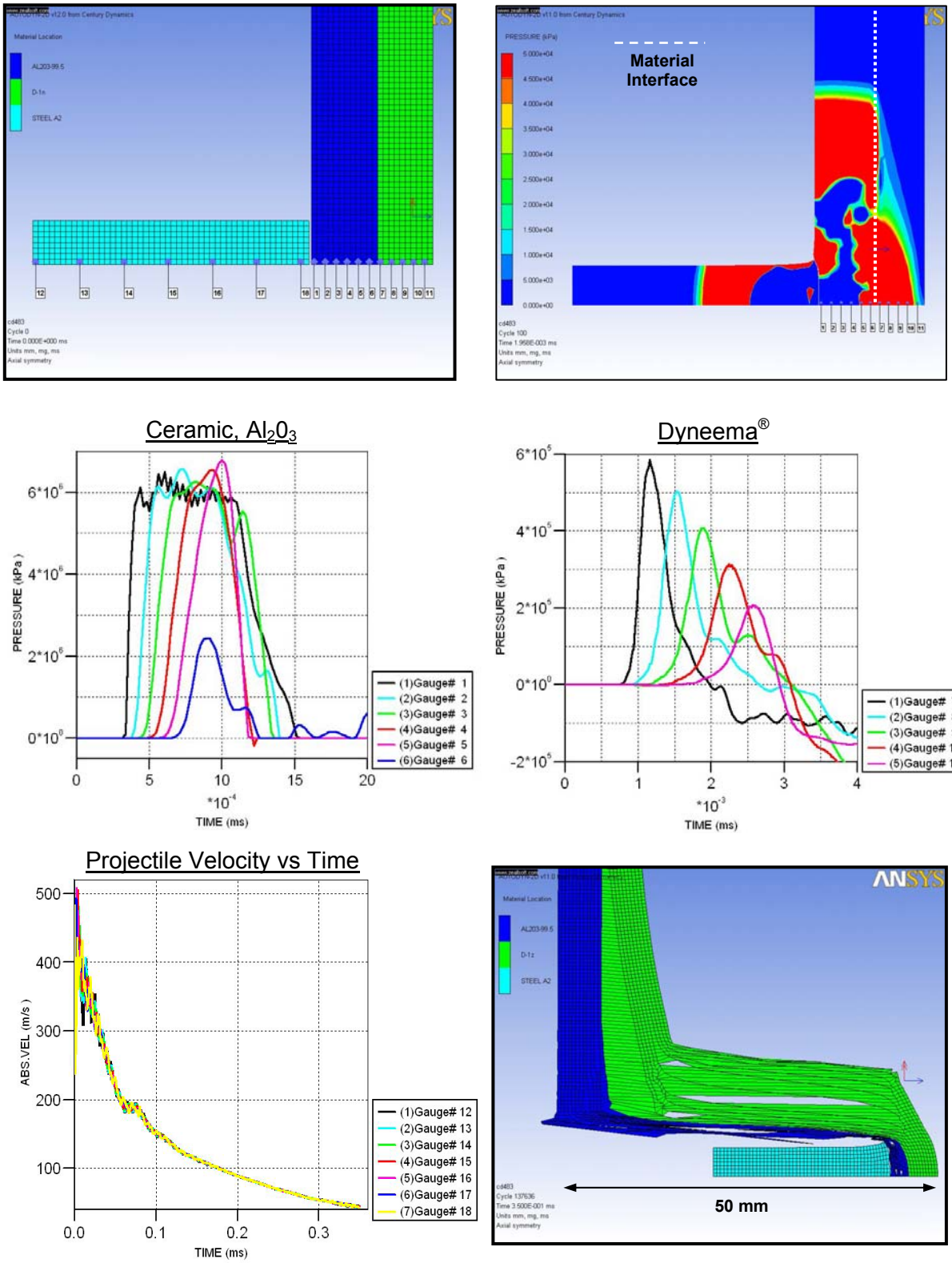

Figure 41. Simulation Results of Shot Number 18

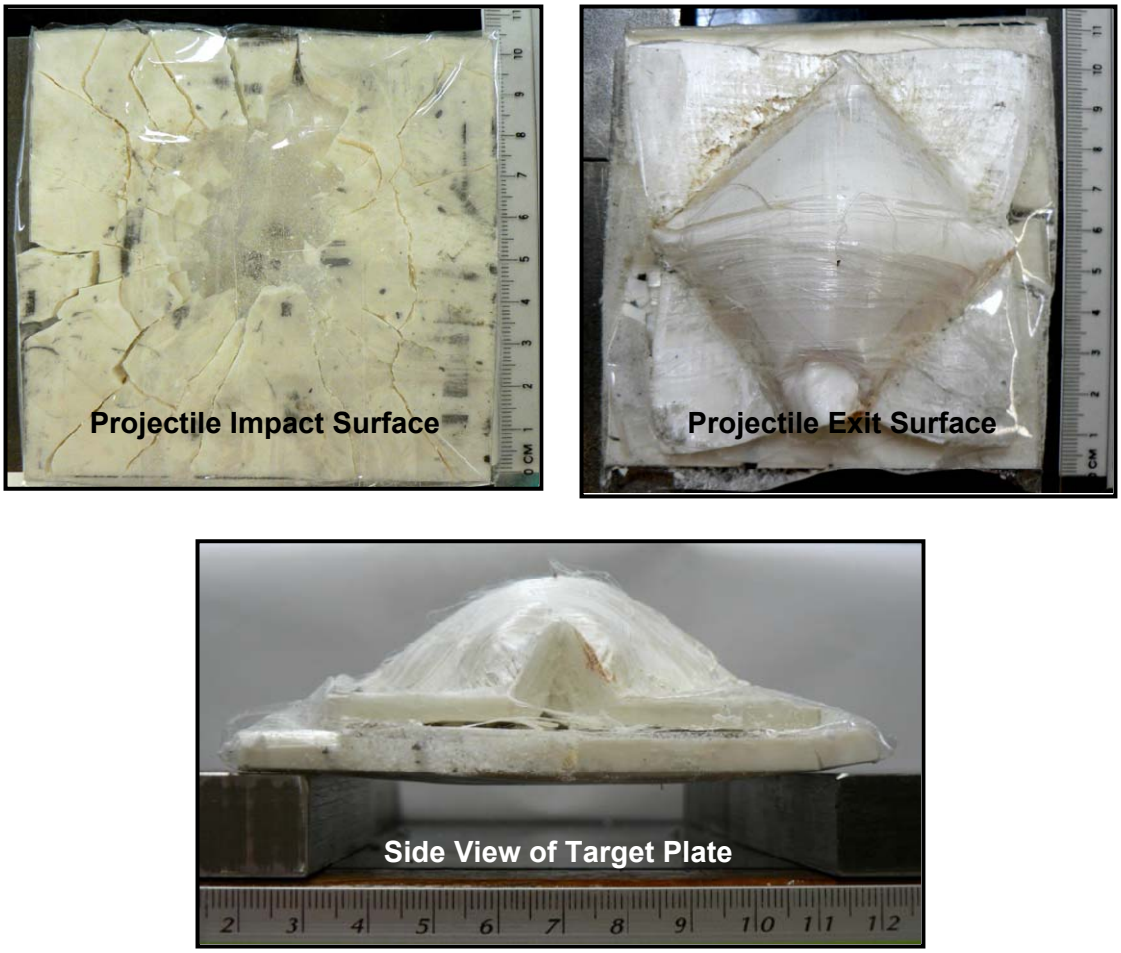

Figure 42. Experimental Results of Shot Number 18

2. Ceramic-Dyneema®-FR6720-Al (C-D-P2-Al) Target Plate

Next, the author looks at a 'complete' composite armor plate. This plate has all the components required to defeat the penetration process discussed earlier. The target plate consists of a 6 mm ceramic layer, a 5mm Dyneema® layer, and a 5 mm FR-6720 polyurethane (PU) foam 0.32 g/cm^3 supported by a thin Aluminum 6061-T6 inertial backing plate to constrain the PU foam. The previous section showed that the inertial backing plate was necessary to confine the porous material so that it could perform its energy absorption role efficiently. As before, the author used a 1" length cylindrical A2 steel projectile. The projectile impacted the target plate at velocity of 463 m/s, according to experimental data.

The stress wave propagation across a structure consisting of dissimilar materials can be extremely complex and may not be easily understood using fundamental shock physics. The impact problem quickly develops into complicated 2D interfacial wave interactions between dissimilar materials. Edge releases of the projectile at the impact interface further complicate this, which destroys the state of uniaxial strain. Therefore, computer codes such as hydrocodes are used to simulate complicated non-linear dynamic problems such as ballistic impacts that cannot be solved analytically. Hence, the performance of the porous foam can only be quantitatively analyzed through its pressure attenuation properties. The simulated pressure plots in Figure 43 clearly show that the compression shock wave was strongly attenuated by the porous material. The pressure was reduced from 0.2 GPa at the last gauge point, namely gauge 11 in the Dyneema® layer to 82 MPa at gauge 16 in the PU foam. This is equivalent to a pressure reduction of 59% across 5 mm of porous foam. Compared to the C-D composite plate configuration, the incorporation of the porous PU foam also increases the stress wave rise time of the propagating stress wave and significantly delays the stress wave propagation. This

effectively spreads out in time the delivery of momentum. The hydrocode simulation predictions capture both the widening rise time and stress wave attenuation characteristics of the porous media.

The author also observed that the plastic collapse and densification of the foam starts at the impact side and is highly localized, while the rest of the porous material remains elastic. The deformation and densification originates from the impact point along the axis of penetration and propagates in the direction perpendicular and traverse to the applied load. Hence, the deformation of the aluminum backing plate can occur only when the foam is fully compacted. This delays the deformation and damage growth in the backing plate and has the potential to improve ballistic performance of the armor.

From the simulation results, the predicted behavior of the laminated target plate under ballistic attack is similar to experimental observations. The author observed typical brittle fracture failure in the ceramic, deformation in the Dyneema® layer, and porous compaction of the PU foam. The composite plate resisted complete penetration in both the simulation and experimental results. The final deformation shape and deflection measurements from the simulation correlates well with experimental results (see Table 7). Figure 44 shows the experimental results for Shot 13. Ong [2] has also demonstrated through impact tests that the ballistic performance of the Dyneema® layer degrades severely without the high-strength ceramic layer. Similarly, the ceramic layer alone has poor ballistic performance as it exhibits extremely brittle fracturing during the impact event. Therefore, it is necessary to adopt a multi-layered armor structure concept for improved ballistic performance.

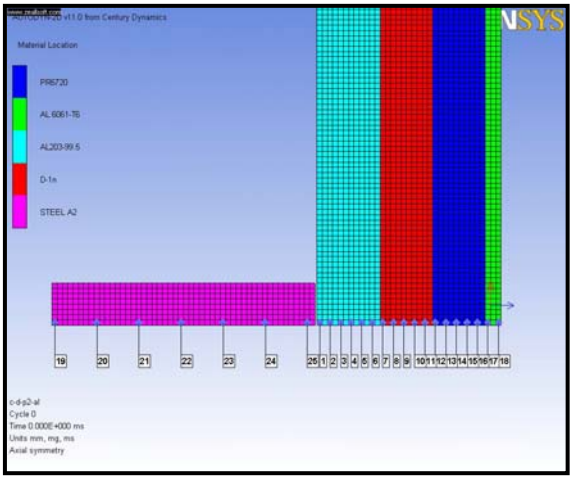

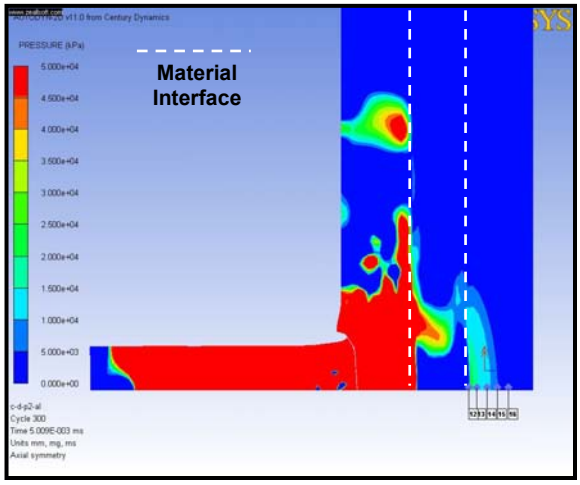

Ceramic, Al_2O_3

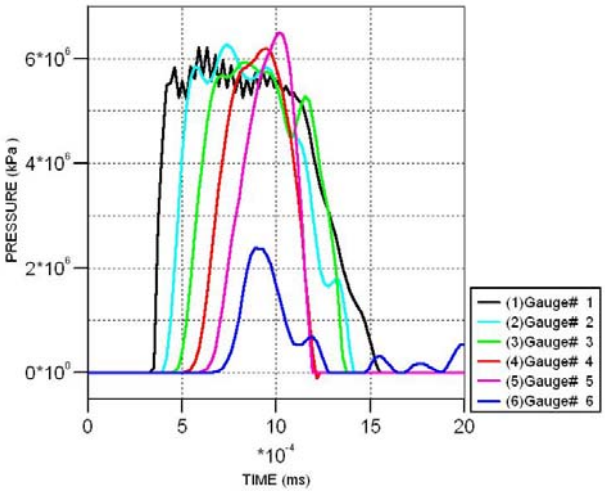

Dyneema®

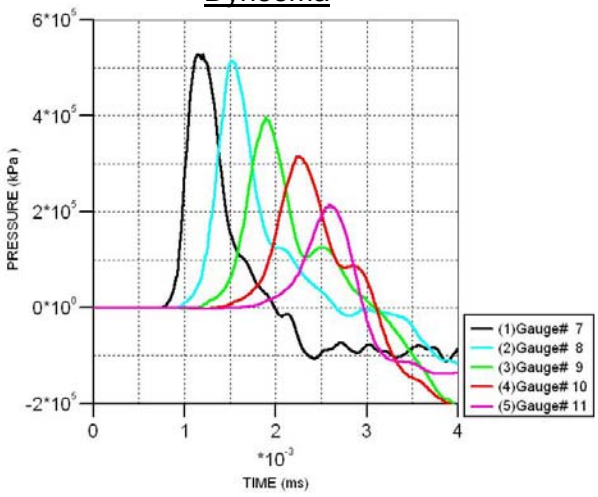

FR-6720 PU Foam

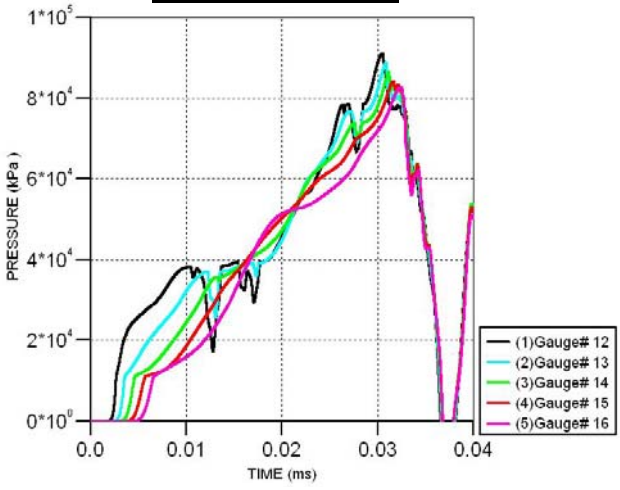

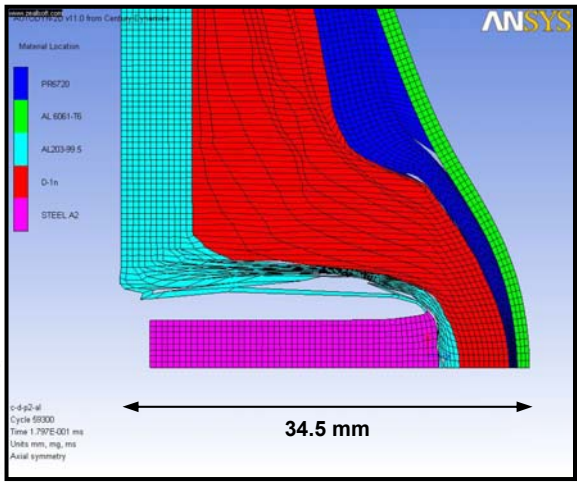

Figure 43. Simulation Results of Shot Number 13

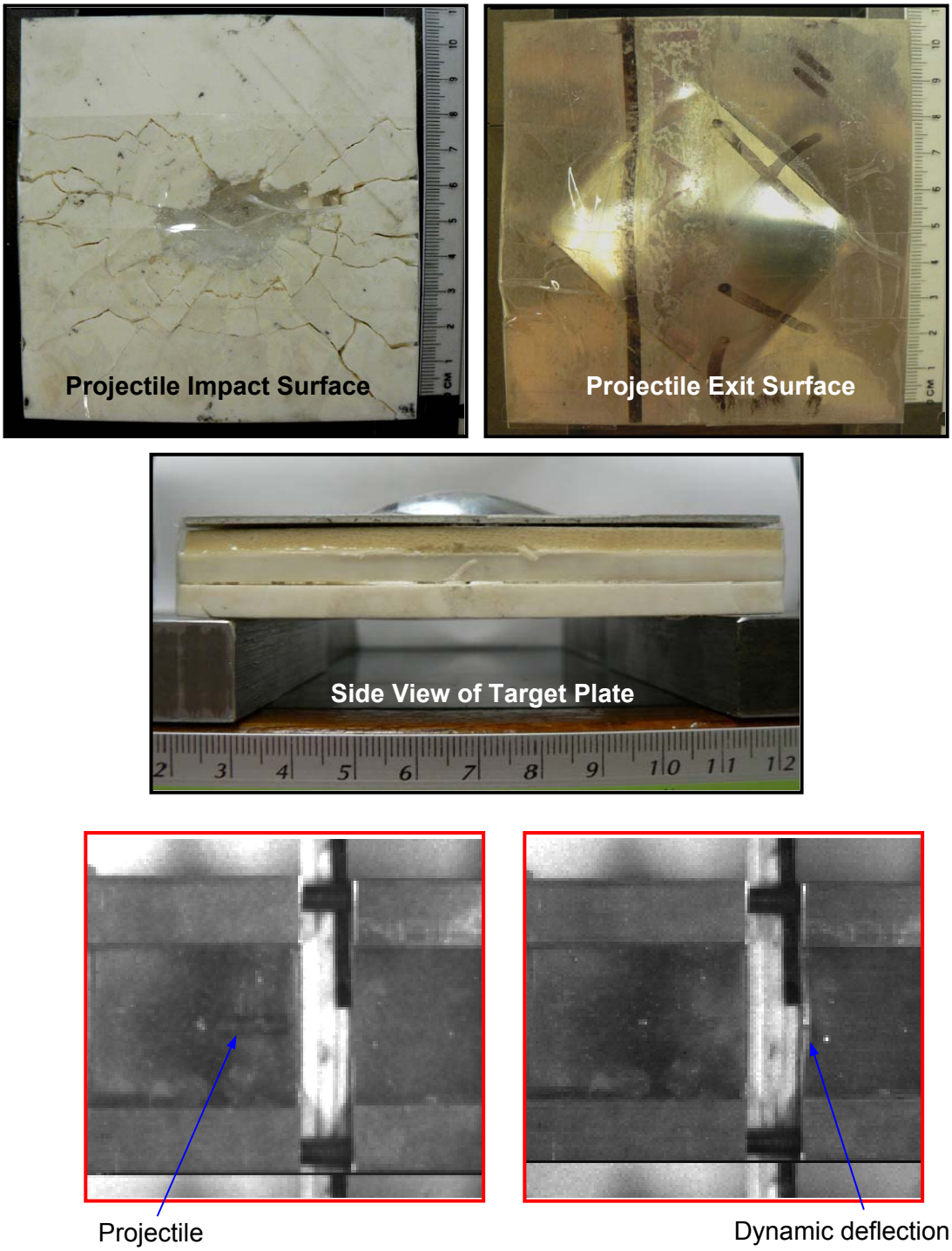

Figure 44. Experimental Results of Shot Number 13

3. Ceramic-Dyneema®-FR6710-Al (C-D-P1-Al) Target Plate

For this system, the target plate consists of a 6 mm ceramic plate, 5 mm Dyneema® layer, and 5 mm FR-6720 polyurethane (PU) foam 0.16 g/cm^3 backed by a thin Aluminium 6061-T6 plate. This is very similar to the test above, but with a lower density PU foam. The measured initial impact velocity of the projectile was 481 m/s. The gauge locations in the simulation setup were as per the C-D-P2-Al target plate.

In general, the failure mechanism is similar to the C-D-P2-Al target plate. Compared to the plate configuration with the more dense foam, the less dense foam more strongly attenuates the compression shock wave (see Figure 45). There was a reduction in pressure from 0.2GPa at the last gauge point, namely gauge 11 in the Dyneema® layer, to 65 MPa at gauge 16 in the PU foam. This is equivalent to a pressure reduction of 67.5% across 5 mm of porous foam. However, the author observed the pressure wave rise time to be shorter than the denser foam. Hence, the damaging compression wave reaches the backing plate earlier than the more dense foam configuration, and backing plate damage deformation and damage growth occurs earlier. The author also observed complete crushing of the foam near the impact point and he observed heavy erosion in the simulations, indicating that the material could have spalled or pulverized. This probably explains the higher dynamic deflection obtained for the C-D-P1-Al target plate deformation. In the actual porous material, micro-cracks can initiate in the brittle porous material if sufficiently large tensile waves are generated.

Figure 46 shows the post-impact condition of the target plate. The author observed similar failure mechanisms as in the test above. This composite plate also resisted complete penetration but with a larger dynamic deflection. The final deformation shape and deflection measurements from the simulation agree reasonably well with experimental results (see Table 7).

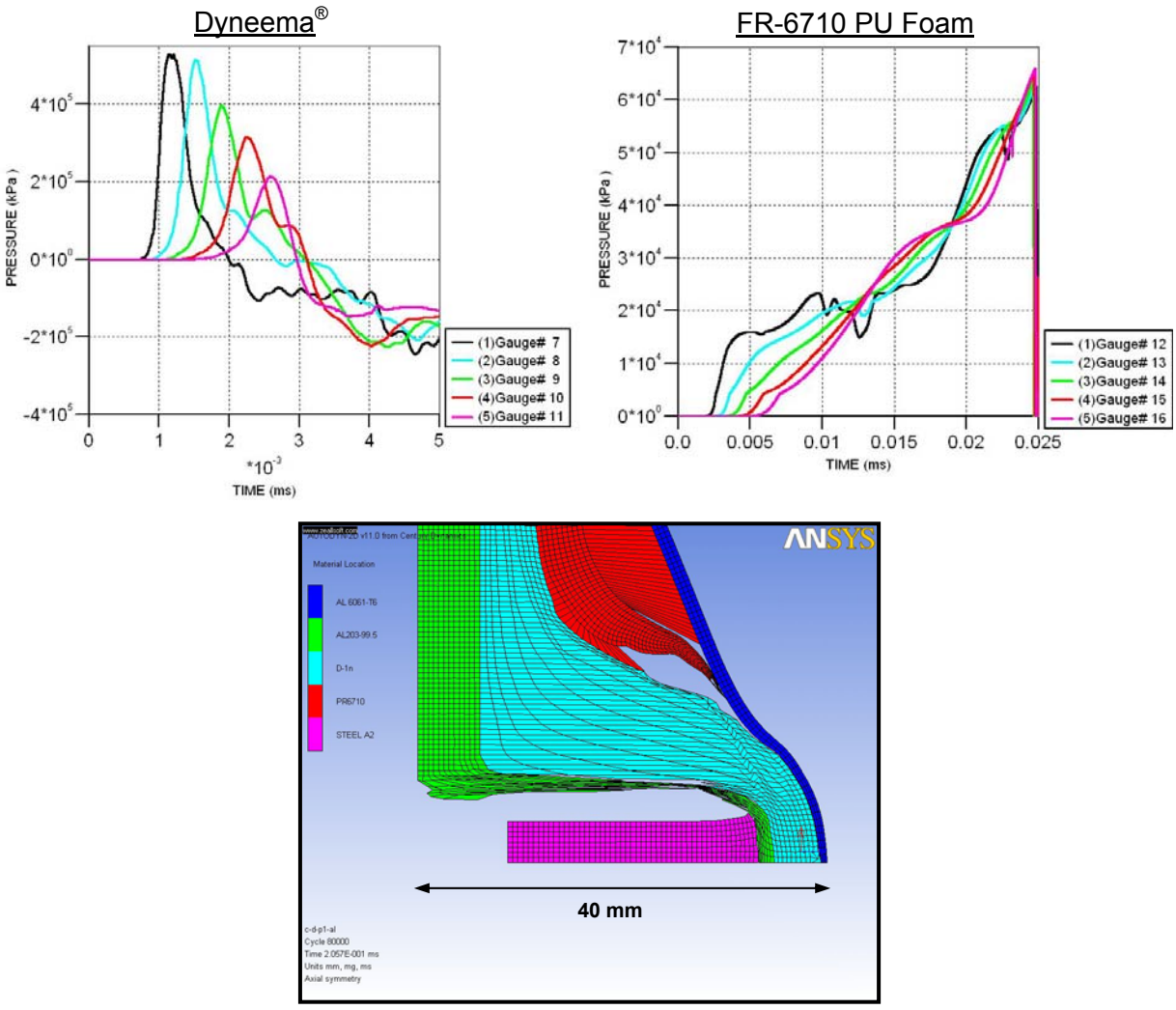

Figure 45. Simulation Results of Shot Number 14

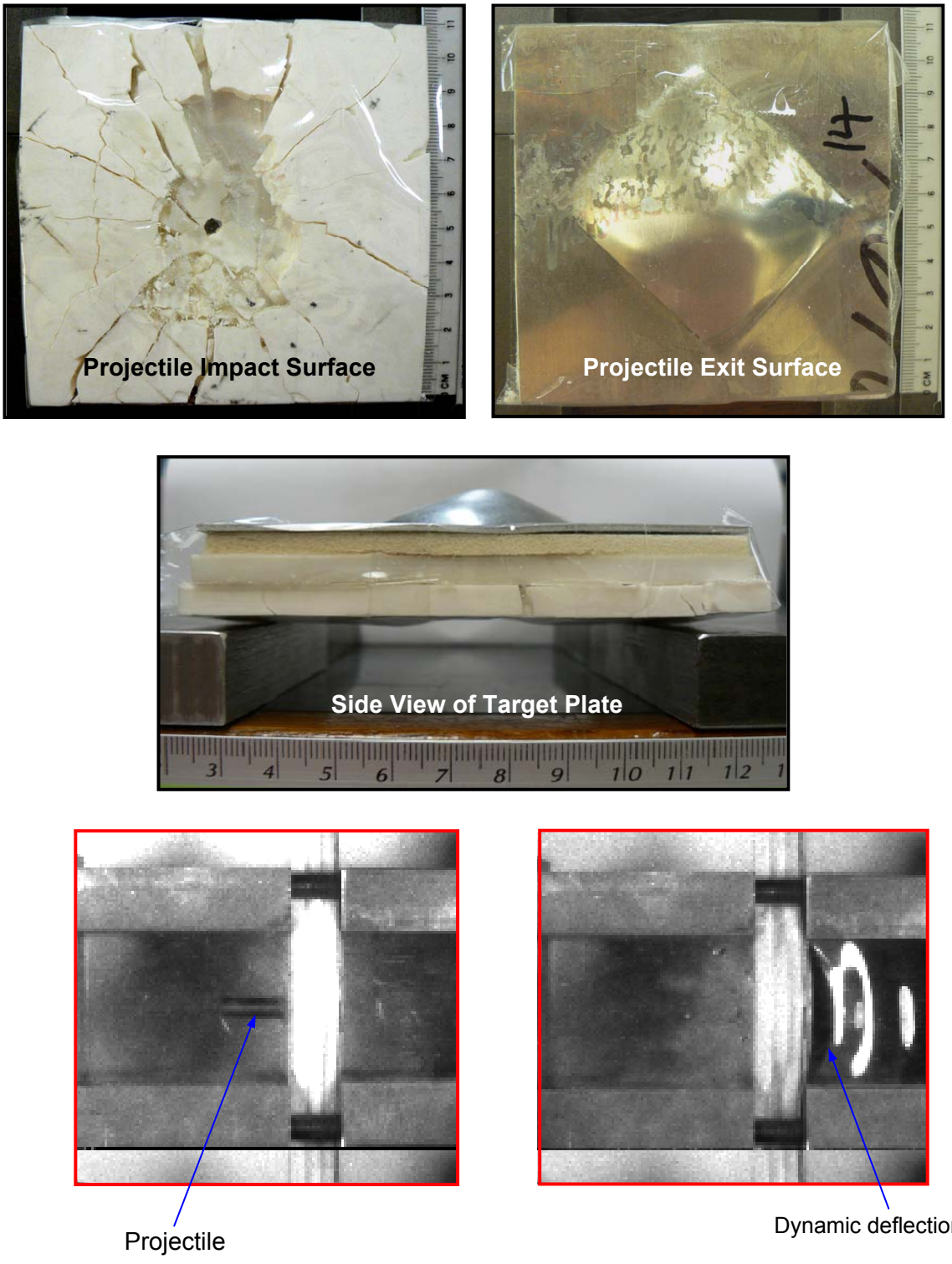

Figure 46. Experimental Results of Shot Number 14

4. Ceramic-Dyneema®-Alulight® AFS (C-D-M) Target Plate

The author modeled the target plate consisting of a 6 mm ceramic, 5 mm Dyneema®, and 12 mm-thick Alulight aluminum foam sandwich (AFS). He measured the projectile as having an initial impact velocity of 465 m/s. The gauge locations in the simulation setup were as per the C-D-P2-Al target plate.

Similar to the other plate configurations with porous materials, the simulation results showed that the porous aluminum strongly attenuates the shock pressure (see Figure 47). There was a reduction in pressure from 0.2 GPa at last gauge point, namely gauge 11 in the Dyneema® layer, to 28 MPa at gauge 20 in the porous aluminum foam. This is equivalent to a pressure reduction of 86% across 5 mm of porous aluminum foam. There is coupling of the strong pressure attenuation with widening of the compression shock rise time, which then introduces significant delay in wave propagation. The air/gas filled cellular structure of the aluminum foam makes stress wave propagation difficult. The cell wall acts as a wave guide and disperses the stress wave. Porous compression is initiated by the cell wall buckling followed by plastic deformation of the cell wall, which then leads to localized densification. The simulation and experimental results showed that the plastic collapse and densification of the foam is highly localized, while the rest of the material remains intact.

Figure 48 shows the post-impact condition of the target plate. As before, the author observes similar failure mechanisms. The composite plate resisted complete penetration with a relatively small dynamic deformation. The final deformation shape and deflection measurements from the simulation correlate well with experimental results (see Table 7).

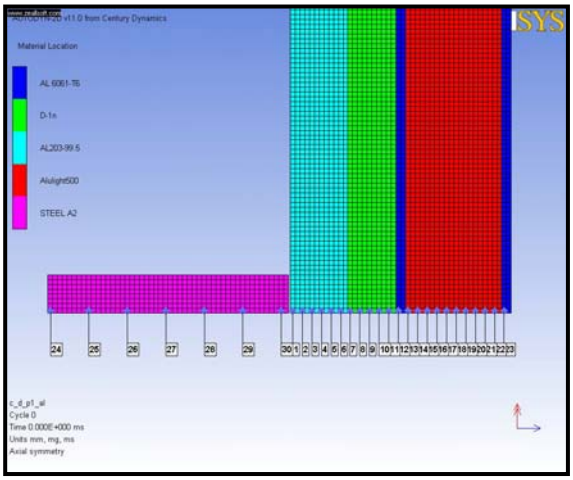

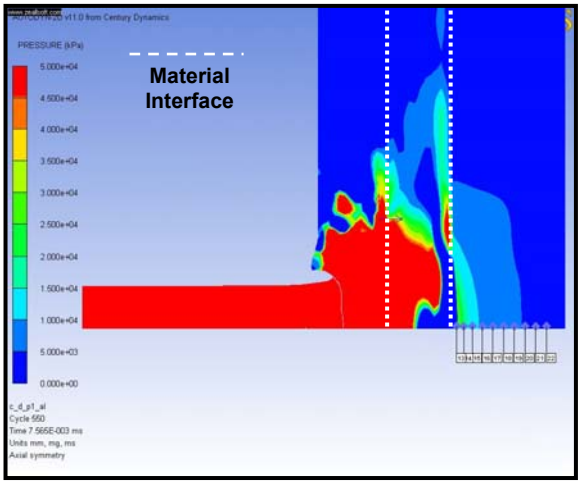

Dyneema®

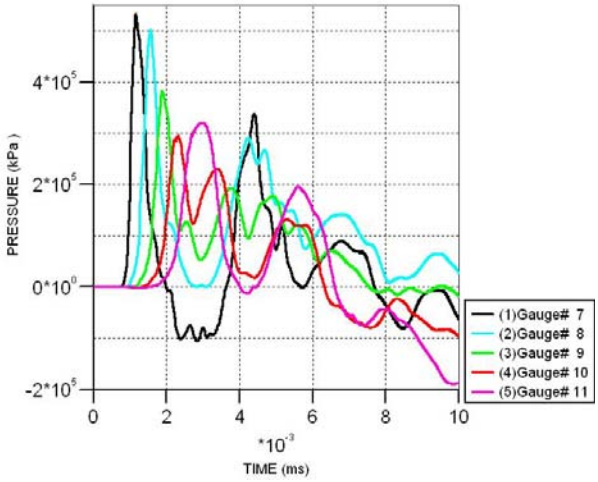

Alulight®500 Metal Foam

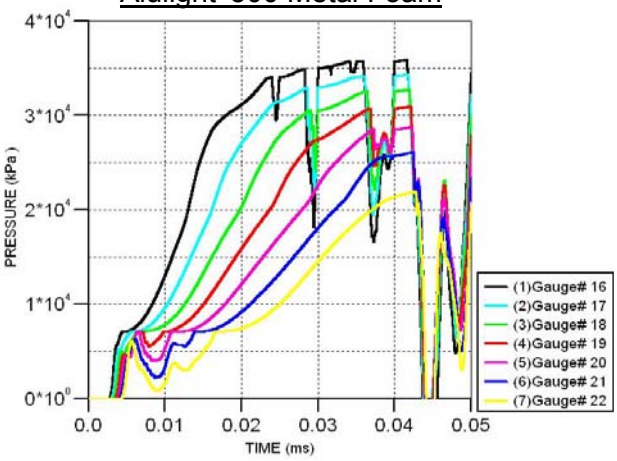

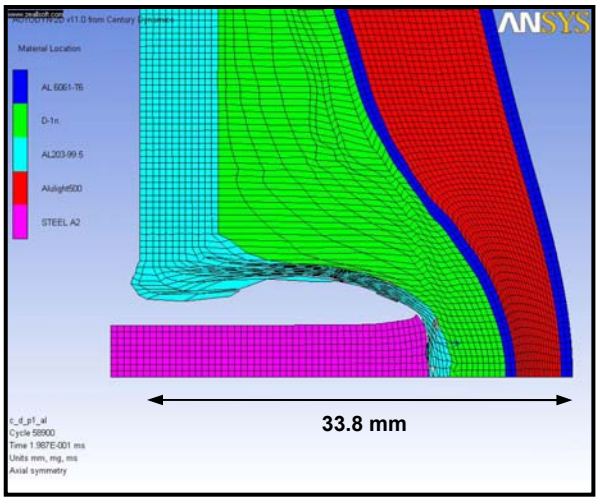

Figure 47. Simulation Results of Shot Number 12

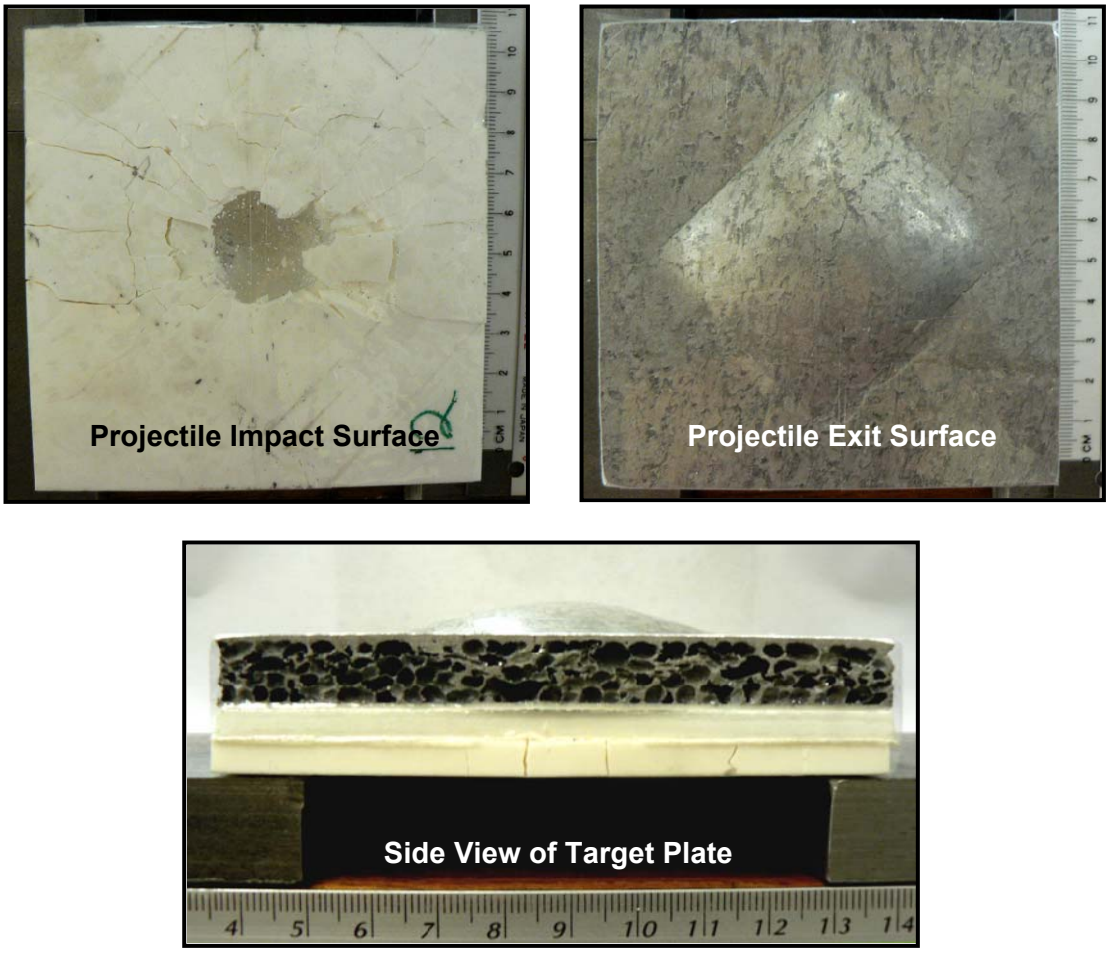

Figure 48. Experimental Results of Shot Number 12

5. Comparison between Simulation and Experiment

Table 7 is a summary of the simulation and experimental.

		Overall Depth, b (mm)		Dynamic Deflection (mm)	
Armor Plate Configuration	**Plate Thickness (mm)**	**Experiment**	**Simulation**	**Experiment**	**Simulation**
C-D	11	45.97	50	34.97	39
C-D-P1-Al	17.5	35.12	40	17.62	22.5
C-D-P2-Al	17.5	32.64	34.5	15.14	17
C-D-M	23	33.57	33.8	10.57	10.8

Legend:

Symbol	Material	Thickness (mm)
Al	Al 6061-T6 Aluminum	1.5
C	Al 203-99.5 Ceramic	6
D	Dyneema	5
M	Alulight aluminum foam sandwich (AFS)	12
P1	FR-6710 rigid polyurethane foam	5
P2	FR-6720 rigid polyurethane foam	5
S	AISI4140 steel	4.76

Table 7. Comparison of Experimental and AUTODYN® results

The AUTODYN® simulations produce results that show a slightly larger deformation as compared with experimental results due to the confinement effects of the experimental setup. In the actual experimental setup, the target plates are clamped in such a way that only an effective area of 50 mm x 50 mm was used. For the author's simulations, the target plate is simulated as 100 mm x 100 mm and hence produces a larger effective area. Therefore, the expectation is for the target to resist penetration for higher projectile speeds if the total effective area of 100 cm^2 is used. However, in general, the characteristics of the simulation results agree relatively well with the experimental results.

From the above results, the C-D armor plate configuration appears to perform worst in terms of dynamic deflection while the C-D-M plate configuration performs best. However, the ballistic performance cannot be ascertained based on the experimental results alone as the impact tests were conducted at varying projectile impact velocities. Since the above simulation results agree well with the experiment, the author can confidently use the simulation model to predict the ballistic performance using a constant projectile impact velocity for a comparison study.

6. Ballistic Performance Comparison Study

In order to perform ballistic performance comparison between the different armor plate configurations, the author performed AUTODYN® simulations using a constant projectile impact velocity of 483 m/s. Figure 49 shows the final deformation shape and deflection measurements for the various armor plate configurations. Figure 50 shows the time taken for the various armor plate configurations to detain the 1" cylindrical steel projectile travelling at 483 m/s. The results show that all four armor designs performed credibly with no projectile perforation. All four armor designs performed better than the benchmarked AISI4140 steel plate (4.76 mm thickness).

From a ballistic performance point of view, it is desirable for the armor plate structure to produce the least dynamic deflection and also be able to arrest the projectile at the shortest possible time. From the simulation results (see Table 8), the C-D-M armor plate configuration has the best overall performance. However, when comparing thicknesses of armor designs, it is important to consider the dynamic thickness, in other words, the summation of static and dynamic thickness [18], which is equivalent to the overall depth b. The areal density or mass effectiveness of the armor design is also a critical metric, as it will affect the overall weight of the armor design. With the two above considerations, the C-D-P2-Al armor plate configuration provides the best overall

performance. Incorporating a porous layer to the armor design improves the performance by 28% compared to the Ceramic-Dyneema® (C-D) composite armor.

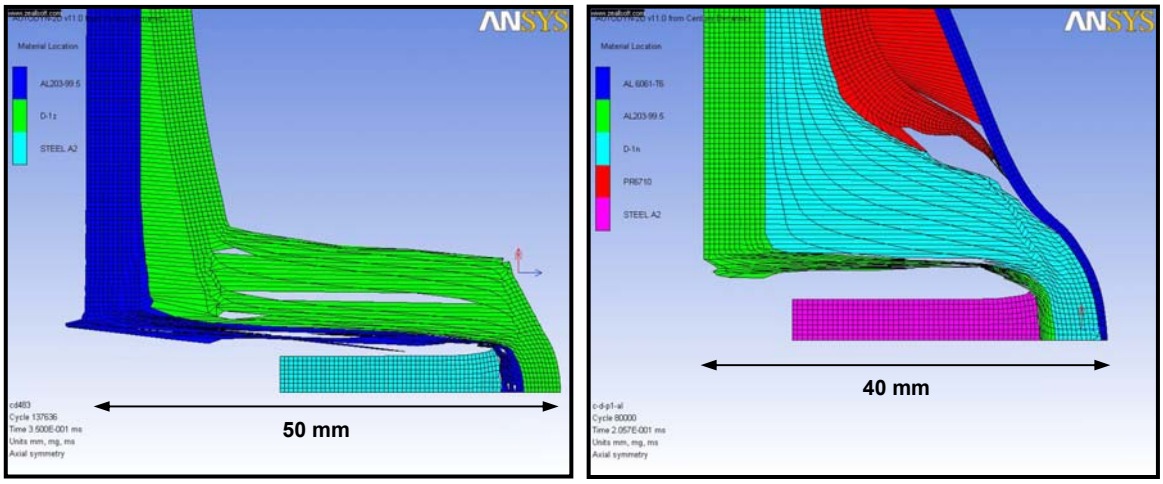

(a) (b)

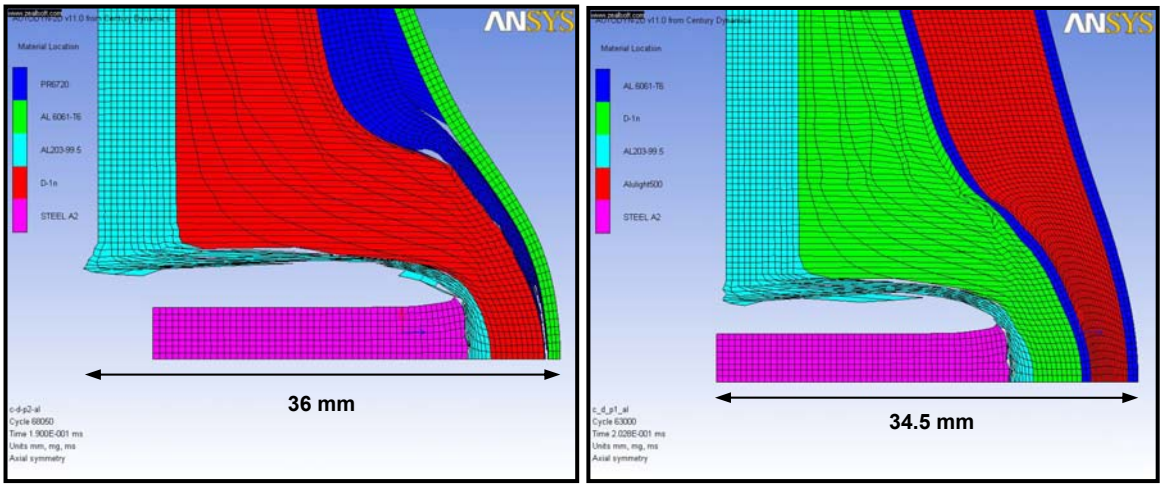

(c) (d)

Figure 49. Simulation Result of a 1" Steel Rod Projectile Impacting (a) C-D; (b) C-D-P1-Al; (c) C-D-P2-Al and (d) C-D-M Target Plate at 483 m/s

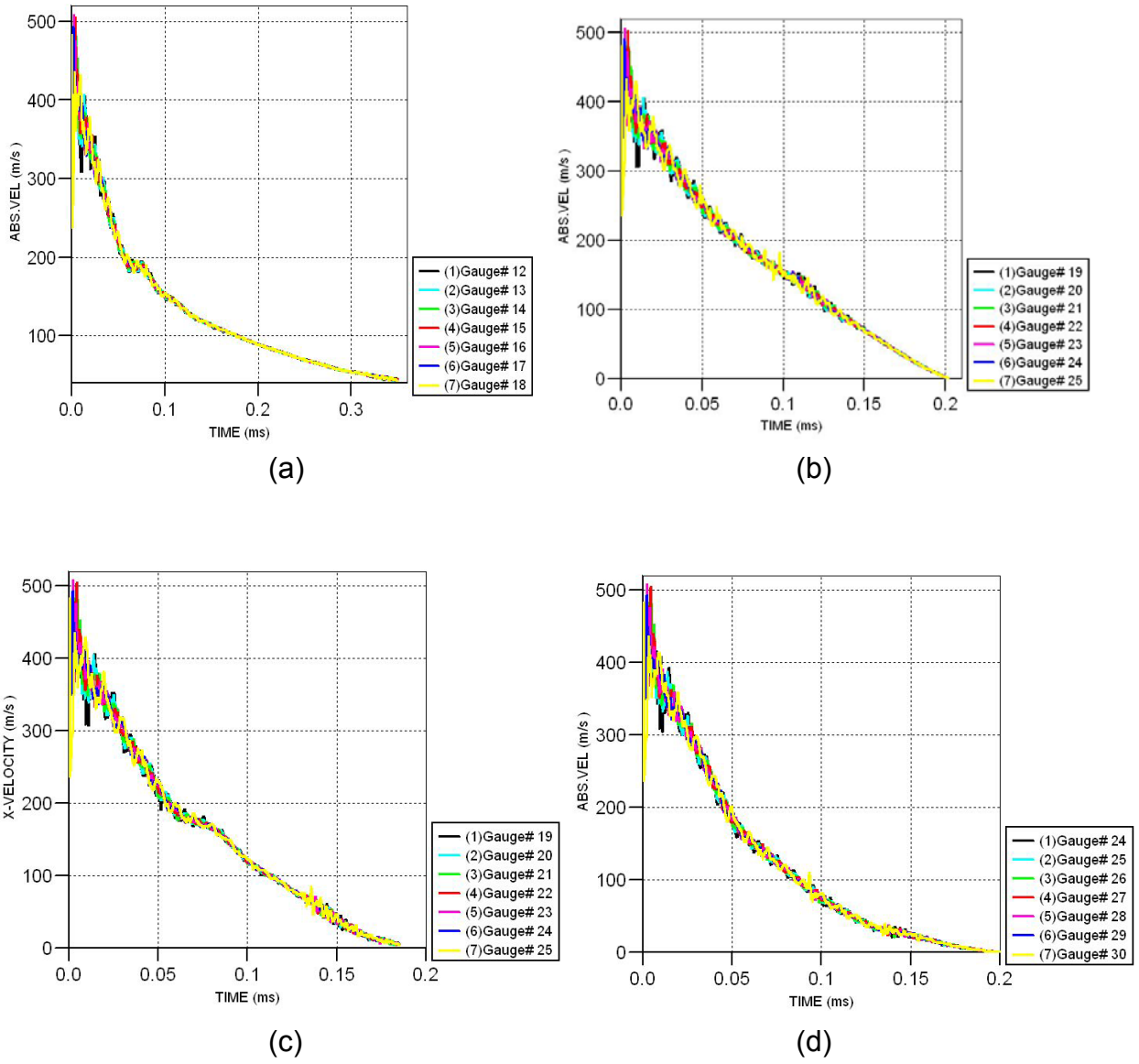

Figure 50. Velocity versus Time Plot for Projectile Impacting (a) C-D; (b) C-D-P1-Al; (c) C-D-P2-Al and (d) C-D-M Target Plate at 483 m/s

Armor Plate Configuration	Areal Density (g/cm^2)	Overall Depth, b (mm)	Dynamic Deflection (mm)	Time taken to arrest projectile (ms)
S	3.737	Complete Penetration		
C-D	2.771	50	39	0.32
C-D-P1-Al	3.256	40	22.5	0.20
C-D-P2-Al	**3.336**	**36**	**18.5**	**0.19**
C-D-M	3.811	34.5	13	0.20
Equivalent Areal Density to C-D-P2-Al Armor Plate				
C-D-P1-Al	3.336	44.5	22	0.22

Legend:

Symbol	Material	Thickness (mm)
Al	Al 6061-T6 Aluminum	1.5
C	Al 203-99.5 Ceramic	6
D	Dyneema	5
M	Alulight aluminum foam sandwich (AFS)	12
P1	FR-6710 rigid polyurethane foam	5
P2	FR-6720 rigid polyurethane foam	5
S	AISI4140 steel	4.76

Table 8. Ballistic Performance Comparison

The author modeled a target plate consisting of a 6 mm ceramic, 5 mm Dyneema®, and 10mm FR-6720 polyurethane (PU) foam 0.16 g/cm^3 backed by a thin Aluminum 6061-T6 plate. This armor plate configuration has the same areal density as the C-D-P2-Al armor plate, and so the author can better compare performance of the two foam materials. The author assigned an initial impact velocity of 483 m/s to the projectile. The objective of this simulation run is to compare the ballistic performance of two porous foams with equal total areal density. Figure 51 shows the simulation results, and it clearly shows that the C-D-P2-Al armor plate configuration still has superior ballistic performance. This result is unexpected as a less dense foam of equivalent areal density is expected to produce larger PV-work due to larger porous volume compression. The simulation results showed complete crushing and severe erosion of the foam near the impact point, indicating that the material could have spalled or

pulverized. This could have impeded the energy absorption performance of the porous material later. There needs to be further investigation to verify the author's predictions and conclusions. Microscopic examination of the impact damage to the porous foam may provide valuable insights.

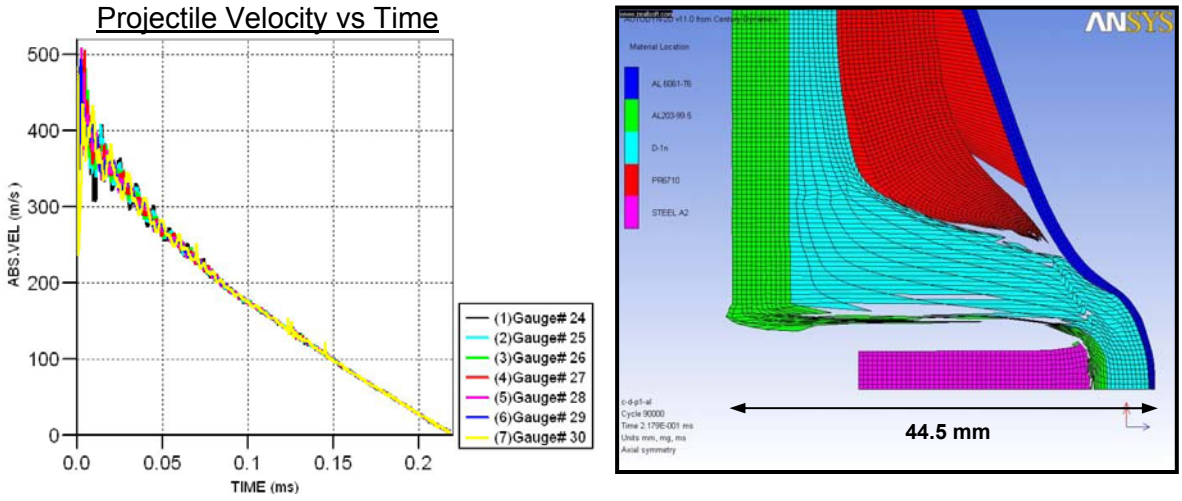

Figure 51. Simulation Results for C-D-P1-Al Armor Plate with 3.336g/cm^2 Areal Density

THIS PAGE INTENTIONALLY LEFT BLANK

VII. CONCLUSIONS AND RECOMMENDATIONS

A. CONCLUSIONS

The current study has shown through both numerical modeling and ballistic trials that a multi-layered armor concept consisting of an initial high strength layer, followed by a second wave-spreading layer, and a shock absorbing third layer of porous material has significantly improved ballistic performance and energy absorption compared to conventional steel armor of equivalent areal density.

In this study, the author developed a material model in AUTODYN® using the porous P-α equation of state compaction model to describe the porous material's behavior when subjected to a transient load such as projectile impact. The P-α compaction model describes initial elastic compression of the porous material due to elastic cell wall buckling, followed by plastic deformation of the cell wall when the applied pressure exceeds the material yield strength. This results in a permanent volume change to the compacted porous material. If the applied pressure continues to increase, the material is dynamically compacted until the applied pressure reaches the fully compacted state, which coincides with the fully dense solid material Hugoniot. Incorporating the porous P-α model with the other material models developed for the above multi-layered armor concept, the simulation studies conducted have shown good agreement with ballistic trial results in terms of material behavior and overall ballistic performance.

The role of the high strength ceramic first layer in an impact event is to deform the projectile and strongly dissipate its energy before it reaches the second layer. The ceramic layer possesses high compressive strength but is not sufficient to stop the projectile on its own due to its brittle fracture behavior. The expectation is for the ceramic material to cause significant plastic deformation of typical small arm ball ammunition, which is made of relatively soft steel core mass. This was not the case for the author's projectiles since they were made of

relatively hard steel that did not deform plastically in a significant manner. The Dyneema® wave-spreading second layer utilizes high wave speed directional fibers to distribute the projectile impact energy laterally and hence, delays the shock wave propagation along the through-thickness of the armor material. The third layer consisting of porous foam has proven to be a good shock attenuator by widening the shock rise time to delay the wave propagation and strongly attenuating the shock wave by absorbing the kinetic energy through compaction of the porous material and turning it into waste heat. This results in reduced dynamic deflection and a shorter time taken to arrest the projectile.

The current study has also clearly proven the necessity of an inertia backing plate to confine the porous material. The role of the inertia backing plate is to prevent the porous material from spalling, which impedes its ability to absorb the impact energy efficiently. Hence, a fourth or final stopping layer consisting of a high strength or penetration resistant material will be essential to serve the function of confining the porous material as well as to provide the final attempt at arresting any penetrator that has penetrated the initial three layers.

In the current research, the author investigated three types of porous materials. Armor solutions containing the porous material layer showed improved ballistic performance compared to a composite plate of Ceramic-Dyneema®. The armor plate configuration that used the more dense polyurethane foam had the best overall performance, achieving a ballistic performance improvement of 28% in terms of dynamic thickness compared to Ceramic-Dyneema® composite armor. The more dense foam configuration (C-D-P2-Al) also had the shortest time to arrest the projectile. Hence, the author can confidently conclude that the attributes of porous materials contribute positively to the weight/performance ratio of the armor system and is an important constituent of the multi-layered armor concept.

The current study has also revealed through analysis of the simulation results that the material characteristics of each layer have been configured to effectively disrupt and absorb the kinetic energy of an incoming penetrator.

Together with ballistic trial results, the author concludes that the sequence of the armor-layering concept is fundamentally correct and has its merits. The enhanced performance with weight minimized is achieved through creative role sharing of multi-functional materials. The superior performance of this innovative, porous foam in an integral layered armor system is a step forward in the design of more damage-tolerant, lightweight personnel and vehicle armor for the future battlefield.

B. RECOMMENDATIONS FOR FUTURE WORK

Since the multi-layered armor concept has proven its benefits, there needs to be more work done to optimize the thickness and performance of each layer. Obtaining a better understanding of fundamental stress wave propagation in dissimilar materials and material failure mechanisms is necessary. Recommended future work includes the following:

1. Measured Properties of Porous Material

Some of the material input properties for simulation input were derived empirically using limited available material information or based on literature research. It is important to perform physical experiments to derive critical material properties such as bulk sound speed, maximum elastic pressure (P_e), and solid compaction pressure (P_s). Ultrasonic tests can measure the bulk sound and the deduction of material strength properties can come from stress-strain behavior tests conducted at high strain rates. With accurate information on material properties, it will be possible to improve the fidelity of the results, and simulations done for weight/performance optimization for armor designs.

2. Performance Against Ogive-shaped Projectile

The basis for current simulation models and experiments are a flat-faced cylindrical projectile. One should perform Numerical modeling using a typical ogive-shaped projectile to replicate actual field applications. The projectile shape

is likely to affect the material behavior in an impact event and hence the overall ballistic performance. A live firing experiment could validate the simulation. The expectation is that the impact velocity of a typical 7.62 mm ball cartridge will reach as high as 900 m/s. The current study, due to limitations of the experimental setup, is limited to impact speeds of 480 m/s for a projectile mass of 8.68 gm.

3. Effect of Pore Structure and Pore Size

In the current research, porous material selection is limited to what is commercially available. Based on the material characterization results performed on the polyurethane foams, the two different foam densities possess similar average pore size and pore size distribution. Future research work on porous material could include studying the materials of same density but with different pore size or cell structure. The study will be able to provide valuable insights on the effect of pore size and structure on energy absorption properties.

LIST OF REFERENCES

[1] C. W. Poh, “Investigation of new materials and methods of construction of personnel armor,” M.S. thesis, Naval Postgraduate School, Monterey, CA, 2008.

[2] C.W. Ong, “Investigation of advanced armor using layered construction,” M.S. thesis, Naval Postgraduate School, Monterey, CA, 2009.

[3] L. J. Gibson and M. F. Ashby, *Cellular Solids: Structure and Properties*. New York: Cambridge University Press, 1997.

[4] K. Kitagawa, et al., “Attenuation Properties of Blast Wave Through Porous Layer,” Shock Waves, 26th *International Symposium on Shock Waves*, vol. 1, pp. 73–78.

[5] R Woodfin, C Schmidt, and M. Banks, “Results of Experiments on Rigid Polyurethane Foam (RPF) for Protection from Mines,” Sandia National Laboratories, Albuquerque, NM, Sandia National Laboratories Rep. SAND98-0645C.

[6] B.A Gama et al., “ Aluminum Foam Integral Armor: A New Dimension in Armor Design,” *Composite Structures*, vol. 52, pp. 381–395, 2001.

[7] Physics of High Velocity Impact, Weapon Lethality, and Survivability, Lecture notes, Naval Postgraduate School, Monterey, CA, 2009.

[8] W. Herrmann, “Constitutive Equation for Dynamic Compression of Ductile Porous Materials,” *J. Appl. Phys.,* vol. 40, pp. 2490–2499, 1969.

[9] M. E. Kipp, et al., “Polyurethane Foam Impact Experiments and Simulations,” *American Physical Society, Conference on Shock Compression of Condensed Matter*, June 28-July 2, 1999.

[10] Century Dynamics, *Users Manual Revision 4.3*, Century Dynamics, 2003.

[11] Century Dynamics, *Theory Manual Revision 4.3*, Century Dynamics 2003.

[12] J.A. Zukas, *Introduction to Hydrocodes*. Missouri: Elsevier Science Ltd., 2004.

[13] D.E. Grady and N.A. Winfree, “A computational model for polyurethane foam,” *Fundamental Issues and Applications of Shock-Wave and High Strain Rate Phenomena*, pp. 485–491, 2001.

[14] M. F. Ashby, et al., “Metal Foams: A Design Guide,” Butterworth-Heinemann Publications, 2000.

[15] General Plastics Manufacturing Company, “LAST-A-FOAM® FR-6700 Aircraft Foam,” *General Plastics Manufacturing Company*. [Online]. Available: http://www.generalplastics.com/products/product_detail.php?pid=15. [Accessed June 2009].

[16] P. Schaeffler, et al., “Production, Properties and Applications of Alulight Closed-Cell Aluminum Foams,” presented at The Fifth International Workshop on Advanced Manufacturing Technologies, London, Canada, 2005..

[17] F. Simancik, W. Rajner, and R. Laag, “Alulight-aluminium foam for lightweight construction”, *SAE 2000 World Congress*, SAE Technical Paper 2000–01–0337, 2000.

[18] B. K. Fink, “Performance metrics for composite integral armor,” *Journal of Thermoplastic Composite Materials,* vol. 13, pp. 417–431, 2000.

INITIAL DISTRIBUTION LIST

1. Defense Technical Information Center
   Ft. Belvoir, Virginia

2. Dudley Knox Library
   Naval Postgraduate School
   Monterey, California

3. Professor Robert S. Hixson
   Physics department
   Naval Postgraduate School
   Monterey, California

4. Professor Terry McNelley
   Department of Mechanical and Astronautical Engineering
   Naval Postgraduate School
   Monterey, California

5. Professor Knox T. Millsaps, Chairman
   Department of Mechanical and Astronautical Engineering
   Naval Postgraduate School
   Monterey, California

6. Professor Yeo Tat Soon
   Director, Temasek Defence Systems Institute
   National University of Singapore
   Singapore

7. Tan Lai Poh (Ms)
   Assistant Manager, Temasek Defence Systems Institute
   National University of Singapore
   Singapore